SHORT REPORT

Selective loss of Purkinje cells in a patient with anti-glutamic acid decarboxylase antibody-associated cerebellar ataxia

Kazuyuki Ishida, Hiroshi Mitoma, Yoshiaki Wada, Teruaki Oka, Junji Shibahara, Yuko Saito, Shigeo Murayama, Hidehiro Mizusawa

J Neurol Neurosurg Psychiatry 2007;**78**:190–192. doi: 10.1136/jnnp.2006.091116

Anti-glutamic acid decarboxylase antibody is associated with the development of progressive cerebellar ataxia and slowly progressive insulin-dependent diabetes mellitus. Previously, the neurophysiological characteristics of IgG in the cerebrospinal fluid of a patient with anti-glutamic acid decarboxylase antibody-associated progressive cerebellar ataxia and slowly progressive insulin-dependent diabetes mellitus were reported. Using a voltage-gated whole-cell recording technique, it was observed that the IgG in the cerebrospinal fluid of the patient selectively suppressed the inhibitory postsynaptic currents in the Purkinje cells. The patient died from aspiration pneumonia. Postmortem examination showed almost complete depletion of the Purkinje cells with Bergmann gliosis. Therefore, the main cause of cerebellar ataxia observed in this case may be attributed to the near-complete depletion of the Purkinje cells. In this paper, the pathomechanisms underlying Purkinje cell damage are discussed.

Glutamic acid decarboxylase (GAD) is a catalytic enzyme that converts glutamic acid to γ-aminobutyric acid, a major inhibitory neurotransmitter. A disease group that is characterised by the presence of a circulating autoantibody against GAD (anti-GAD antibody) includes the following: slowly progressive insulin-dependent diabetes mellitus (SPIDDM), stiff-person syndrome (SPS) and progressive cerebellar ataxia (PCA).[1–3] Anti-GAD antibody is one of the serological diagnostic markers of these diseases. Honnorat *et al*[4] reported a significant link between the anti-GAD antibody and cerebellar ataxia after screening 9000 serum samples. In addition, autoimmune mechanisms against GAD are presumed to be the causative agents of these diseases.[5] Here, we report the autopsy findings of PCA with anti-GAD antibody and discuss the pathomechanism of this rare disease.

CASE REPORT

We previously reported part of the clinical course of a patient with PCA and SPIDDM, and showed the neurophysiological characteristics of IgG in the cerebrospinal fluid.[6] In September 1996, a 66-year-old woman developed cerebellar ataxia of the limbs and trunk. In April 1997, she had sudden onset of hyperglycaemia, and was subsequently diagnosed with anti-GAD-associated SPIDDM. In May 1997, she was bedridden due to severe cerebellar ataxia; other symptoms such as extrapyramidal or pyramidal tracts were not observed. The patient was diagnosed with anti-GAD antibody-associated PCA, and received four rounds of plasma exchange and immunosuppressive treatment. After treatment, the patient showed slight improvement in cerebellar ataxia.

In December 2000, the patient experienced painful spasms and rigidity in the trunk that mimicked symptoms of SPS. Diazepam and baclofen were effective in ameliorating the severe pain associated with the spasms and rigidity. The painful spasms subsided spontaneously within 2 months. The patient died of aspiration pneumonia in October 2001.

During the 5-year clinical course, repeated neuroradiological examinations showed no significant cerebellar atrophy. Using a voltage-gated whole-cell recording technique, we observed that the IgG in the cerebrospinal fluid of the patient, selectively suppressed the inhibitory postsynaptic currents in the Purkinje cells.[6 7]

Postmortem examination

Postmortem examination was performed 22 h after death. The brain weighed 1150 g. The brain and the entire spinal cord were fixed in formalin and prepared for a morphological examination. Macroscopically, there was no atrophy of the cerebrum, brain stem, cerebellum (fig 1A) and spinal cord. The representative areas were examined by routine and immunohistochemical staining, as reported previously.[8] In short, 6-μm thick serial sections were stained with haematoxylin and eosin, Klüver–Barrera and Bodian silver staining. For the immunohistochemical study, 6-μm dewaxed and microwave-irradiated sections were stained using a Ventana 20NX automatic stainer (Ventana, Tucson, Arizona, USA). Microscopical examination showed almost complete depletion of the Purkinje cells and diffuse proliferation of the Bergmann glia (fig 1B). The number of remaining Purkinje cells was no more than one per cerebellar folium. Bodian staining showed multiple empty baskets (fig 1C). There was no specific inflammatory response, and the other structures of the central nervous system, including the cerebral cortex, white matter, basal ganglia, brain stem and spinal cord, did not show marked pathological changes. The pancreas showed a definite and marked decrease in the islets in the tail (fig 1D), and lymphocytic infiltration in the islets situated in the pancreatic body.

DISCUSSION

The selective loss of both Purkinje cells and pancreatic islets was a characteristic finding in this case. The selective degeneration of the Purkinje cells partially mimics the pathological changes observed in paraneoplastic cerebellar ataxia associated with anti-mGluR1 or anti-Yo antibody; however, the exclusive pathological changes related to the Purkinje cells constitute a unique feature of this case.[9 10] On the other hand, the lymphocytic infiltration in the pancreas and the selective decrease in the pancreatic islets corresponded with the pathological findings of autoimmune insulin-dependent diabetes mellitus.[11] Therefore, the main causes of cerebellar ataxia and diabetes mellitus seem to be related to the depletion of the Purkinje cells and the decrease in the pancreatic islets,

Abbreviations: GAD, glutamic acid decarboxylase; PCA, progressive cerebellar ataxia; SPIDDM, slowly progressive insulin-dependent diabetes mellitus; SPS, stiff-person syndrome

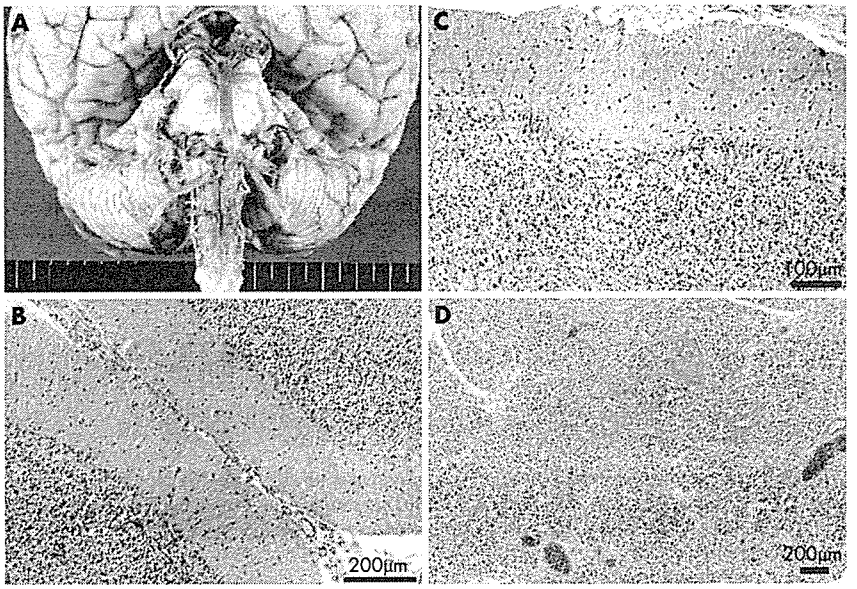

Figure 1 (A) Macroscopic appearance of the brain stem and cerebellum. There are no atrophic changes in the cerebellum and brain stem. (B) Haematoxylin and eosin staining of the cerebellar cortex. There is severe depletion of Purkinje cells and proliferation of Bergmann glia. (C) Bodian staining of the cerebellar cortex. Multiple empty baskets can be observed. (D) Pancreatic tail (haematoxylin and eosin staining). There is a selective decrease in the pancreatic islets.

respectively. To our knowledge, this is the first autopsy report of PCA associated with anti-GAD antibody.

Immunohistochemical staining using anti-GAD and anti-calbindin antibodies failed to react with the patient's specimen; this indicated a complete loss of antigenicity in the patient's specimen, due to postmortem delay and excessive fixation. Therefore, it became difficult to analyse the morphological changes in the other GAD-containing neurones, such as the cerebellar basket cells and the spinal Renshaw cells. However, the existence of multiple empty baskets suggested that, in contrast to the Purkinje cells that were lost, the basket cells were relatively preserved.[12]

We inferred two possible pathomechanisms to explain the Purkinje cell damage: indirect and direct immune-mediated mechanisms. The indirect mechanism might be associated with excitotoxicity of the Purkinje cells by the selective suppression of inhibitory postsynaptic currents and the attenuation of inhibition of excitatory postsynaptic currents by the anti-GAD antibody.[6 7 13] The direct mechanism might be mediated by cytotoxic reactions against the Purkinje cells caused by the invading leucocytes, as observed in the pancreatic islets. However, it is presently unclear whether the mechanisms that are more likely to have caused the Purkinje cell damage are indirectly or directly immune-mediated.

The patient experienced painful muscle spasms that mimic symptoms of SPS. The muscle spasms observed in SPS are considered to occur as a result of the dysfunction of the Renshaw cells that are γ-aminobutyric acid inhibitory interneurones in the spinal cord.[14] Various pathological changes are observed in the spinal cord of patients with SPS; however, lymphocytic cuffing and a decrease in the number of anterior horn neurones are considered to be representative of SPS.[15] In contrast, the pathological changes observed in our patient were unremarkable; this suggests that the Renshaw cells were not severely damaged. This may explain the transient nature of the muscular spasms in this case.

Based on the quantitative analysis of the brain autopsy of a patient with SPS and without cerebellar ataxia, Warich-Kirches *et al*[16] reported diminished cell density of the inhibitory neurones in the cerebellar cortex. Combining their case results with ours might show the phenotypic overlap of the anti-GAD autoimmunity-associated neurological diseases.

Authors' affiliations
Kazuyuki Ishida*, Department of Neurology, Tamagawa Hospital, Setagaya-ku, Tokyo, Japan
Hiroshi Mitoma, Mitoma Neurological Clinic, Shinjuku-ku, Tokyo, Japan
Yoshiaki Wada, Department of Rehabilitation, Tamagawa Hospital, Setagaya-ku, Tokyo, Japan
Teruaki Oka, Department of Pathology, Kanto Central Hospital, Setagaya-ku, Tokyo, Japan
Junji Shibahara, Department of Pathology, University of Tokyo, Bunkyo-ku, Tokyo, Japan
Yuko Saito, Shigeo Murayama, Department of Neuropathology, Tokyo Metropolitan Institute of Gerontology, Itabashi-ku, Tokyo, Japan
Hidehiro Mizusawa, Department of Neurology and Neurological Science, Tokyo Medical and Dental University Graduate School, Bunkyo-ku, Tokyo, Japan

Competing interests: None declared.

Informed consent was obtained from the family of the patient for the publication of her details in this paper.

Correspondence to: Dr Kazuyuki Ishida, Institute of Oriental Medicine, Tokyo Women's Medical University, School of Medicine, 4th floor, Shinjuku NS Building, 2-4-1 Nishi-Shinjuku, Shinjuku-ku, Tokyo 163-0804, Japan; k-ishida@iom.twmu.ac.jp

Received 17 February 2006
Revised 13 October 2006
Accepted 25 October 2006
Published Online First 17 November 2006

REFERENCES

1 **Seissler J**, Amann J, Mauch L, *et al*. Prevalence of autoantibodies to the 65- and 67-kD isoforms of glutamate decarboxylase in insulin-dependent diabetes mellitus. *J Clin Invest* 1993;**92**:1394–9.
2 **Saiz A**, Arpa J, Sagasta A, *et al*. Autoantibodies to glutamic acid decarboxylase in three patients with cerebellar ataxia, late-onset insulin-dependent diabetes mellitus, and polyendocrine autoimmunity. *Neurology* 1997;**49**:1026–30.
3 **Vianello M**, Tavolato B, Giometto B. Glutamic acid decarboxylase autoantibodies and neurological disorders. *Neurol Sci* 2002;**23**:145–51.
4 **Honnorat J**, Saiz A, Giometto B, *et al*. Cerebellar ataxia with anti-glutamic acid decarboxylase antibodies: study of 14 patients. *Arch Neurol* 2001;**58**:225–30.
5 **Dalakas MC**, Li M, Fujii M, *et al*. Stiff person syndrome: quantification, specificity, and intrathecal synthesis of GAD65 antibodies. *Neurology* 2001;**57**:780–4.
6 **Ishida K**, Mitoma H, Song SY, *et al*. Selective suppression of cerebellar GABAergic transmission by an autoantibody to glutamic acid decarboxylase. *Ann Neurol* 1999;**46**:263–7.

7 **Mitoma H**, Song SY, Ishida K, *et al.* Presynaptic impairment of cerebellar inhibitory synapses by an autoantibody to glutamate decarboxylase. *J Neurol Sci* 2000;**175**:40–4.
8 **Saito Y**, Suzuki K, Nanba E, *et al.* Niemann-Pick type C disease: accelerated neurofibrillary tangle formation and amyloid beta deposition associated with ApoE e4 homozygosity. *Ann Neurol* 2002;**52**:351–5.
9 **Coesmans M**, Smitt PA, Linden DJ, *et al.* Mechanisms underlying cerebellar motor deficits due to mGluR1-autoantibodies. *Ann Neurol* 2003;**53**:325–36.
10 **Verschuuren J**, Chuang L, Rosenblum MK, *et al.* Inflammatory infiltrates and complete absence of Purkinje cells in anti-Yo-associated paraneoplastic cerebellar degeneration. *Acta Neuropathol (Berl)* 1996;**91**:519–25.
11 **Nakanishi K**, Kobayashi T, Miyashita H, *et al.* Relationships among residual beta cells, exocrine pancreas, and islet cell antibodies in insulin-dependent diabetes mellitus. *Metabolism* 1993;**42**:196–203.
12 **Gatti RA**, Vinters HV. Cerebellar pathology in ataxia-telangiectasia: the significance of basket cells. *Kroc Found Ser* 1985;**19**:225–32.
13 **Mitoma H**, Ishida K, Shizuka-Ikeda M, *et al.* Dual impairment of GABAA- and GABAB-receptor-mediated synaptic responses by autoantibodies to glutamic acid decarboxylase. *J Neurol Sci* 2003;**208**:51–6.
14 **Meinck HM**, Ricker K, Hulser PJ, *et al.* Stiff man syndrome: clinical and laboratory findings in eight patients. *J Neurol* 1994;**241**:157–66.
15 **Warren JD**, Scott G, Blumbergs PC, *et al.* Pathological evidence of encephalomyelitis in the stiff man syndrome with anti-GAD antibodies. *J Clin Neurosci* 2002;**9**:328–9.
16 **Warich-Kirches M**, Von Bossanyi P, Treuheit T, *et al.* Stiff-man syndrome: possible autoimmune etiology targeted against GABA-ergic cells. *Clin Neuropathol* 1997;**16**:214–19.

Human Molecular Genetics, 2006, Vol. 15, No. 7 *1151–1158*
doi:10.1093/hmg/ddl030
Advance Access published on February 24, 2006

Multiple candidate gene analysis identifies α-*synuclein* as a susceptibility gene for sporadic Parkinson's disease

Ikuko Mizuta[1], Wataru Satake[1], Yuko Nakabayashi[1,2], Chiyomi Ito[1,2], Satoko Suzuki[1,2], Yoshio Momose[1,†], Yoshitaka Nagai[1], Akira Oka[3], Hidetoshi Inoko[3], Jiro Fukae[4], Yuko Saito[5,6], Motoji Sawabe[5], Shigeo Murayama[6], Mitsutoshi Yamamoto[7], Nobutaka Hattori[4], Miho Murata[8] and Tatsushi Toda[1,2,*]

[1]Division of Clinical Genetics, Department of Medical Genetics, Osaka University Graduate School of Medicine, 2-2-B9 Yamadaoka, Suita, Osaka 565-0871, Japan, [2]Core Research for Evolutional Science and Technology (CREST), Japan Science and Technology Agency, Saitama 332-0012, Japan, [3]Department of Molecular Life Science, Tokai University School of Medicine, Kanagawa 259-1193, Japan, [4]Department of Neurology, Juntendo University School of Medicine, Tokyo 113-8421, Japan, [5]Department of Pathology, Tokyo Metropolitan Geriatric Hospital, Tokyo 173-0015, Japan, [6]Department of Neuropathology, Tokyo Metropolitan Institute of Gerontology, Tokyo 173-0015, Japan, [7]Department of Neurology, Kagawa Prefectural Central Hospital, Takamatsu 760-8557, Japan and [8]Department of Neurology, Musashi Hospital, National Center of Neurology and Psychiatry, Tokyo 187-8551, Japan

Received December 22, 2005; Revised and Accepted February 15, 2006

Parkinson's disease (PD), one of the most common human neurodegenerative diseases, is characterized by the loss of dopaminergic neurons in the substantia nigra of the midbrain. PD is a complex disorder with multiple genetic and environmental factors influencing disease risk. To identify susceptible genes for sporadic PD, we performed case–control association studies of 268 single nucleotide polymorphisms (SNPs) in 121 candidate genes. In two independent case–control populations, we found that a SNP in α-*synuclein* (*SNCA*), rs7684318, showed the strongest association with PD ($P = 5.0 \times 10^{-10}$). Linkage disequilibrium (LD) analysis using 29 SNPs in a region around rs7684318 revealed that the entire *SNCA* gene lies within a single LD block ($D' > 0.9$) spanning ~120 kb. A tight LD group ($r^2 > 0.85$) of six SNPs, including rs7684318, associated most strongly with PD ($P = 2.0 \times 10^{-9}$–1.7×10^{-11}). Haplotype association analysis did not show lower *P*-values than any single SNP within this group. SNCA is a major component of Lewy bodies, the pathological hallmark of PD. Aggregation of SNCA is thought to play a crucial role in PD. *SNCA* expression levels tended to be positively correlated with the number of the associated allele in autopsied frontal cortices. These findings establish *SNCA* as a definite susceptibility gene for sporadic PD.

INTRODUCTION

Sporadic Parkinson's disease (PD) (OMIM no. 168600) is the second most common neurodegenerative disease following Alzheimer's disease. PD is late onset and progressive, affecting 1–2% of persons older than 65 years. Clinical features of PD include resting tremor, bradykinesia, rigidity and postural instability. The disease is pathologically characterized by the loss of dopaminergic neurons in the substantia nigra and the presence of intracellular inclusions known as Lewy bodies. Various medical managements are available for PD, including drugs (l-dopa, dopamine agonists, anti-cholinergic drugs, etc.) and surgery (thalamotomy, pallidotomy, deep brain stimulation, etc.) (1). These treatments improve PD symptoms, but do little to deter disease progression. Identifying risk factors for PD can be helpful in delaying disease onset and slowing its progression.

*To whom correspondence should be addressed. Tel: +81 668793380; Fax: +81 668793389; Email: toda@clgene.med.osaka-u.ac.jp
†Present address: Department of Clinical Bioinformatics, Graduate School of Medicine, University of Tokyo, Tokyo 113-8655, Japan.

PD is a complex common disease, caused by multiple genetic and environmental factors (2). The contribution of genetic factors to sporadic PD is indicated by several findings. First, ~10% of patients with PD have a positive family history (3). Secondly, a recent large-scale survey in Iceland showed that the risk ratio for PD was increased in related individuals (6.7 for siblings, 3.2 for offspring and 2.7 for nephews and nieces of patients with PD) (4). Thirdly, a twin study using [^{18}F]dopa PET showed that the concordance rate for PD, including subclinical cases, is approximately three times higher in monozygotic twins (55%) than in dizygotic twins (18%) (5).

Causal genes for Mendelian-inherited PD have been reported, including *α-synuclein* [4q21, autosomal dominant (AD)] (6), *parkin* [6q25.2–27, autosomal recessive (AR)] (7), *UCH-L1* (4p14, AD) (8), *PINK1* (1p36, AR) (9), *DJ-1* (1p36, AR) (10), *LRRK2/dardarin* (12q12, AD) (11,12) and *NR4A2/Nurr1* (2q22–23, AD) (13).

Many case–control association studies using single nucleotide polymorphisms (SNPs) in candidate genes have been reported, but few consistent findings have been obtained (2). This is due, in part, to limited numbers of available samples, target genes and/or genetic markers. Since 2001, genome-wide, non-parametric linkage analysis of PD families has revealed significant linkage in multiple chromosomal regions (14–17), leading to the identification of *tau* (18) and *FGF20* (19) as susceptibility genes.

To date, polymorphisms that influence PD as strongly as *APOE-ε4* influences Alzheimer's disease have not been identified. Through extensive candidate gene association studies, we have established *α-synuclein* (*SNCA*) as a definite susceptibility gene for sporadic PD.

RESULTS

Screening of SNPs in candidate genes for PD

We selected candidate genes from the literature describing genetic, pathological and biochemical findings in PD, as well as genes that participate in the proposed mechanisms for PD. Finally, we picked up 121 genes relevant to familial PD, Lewy bodies, dopaminergic neurons, cytokines and trophic factors, mitochondrial functions, oxidative stress, proteasome function, autophagy, endoplasmic reticulum-associated degradation (ERAD) and toxins. One to seven SNPs per gene (268 SNPs total) were selected from the dbSNP, JSNP and Celera Discovery System databases.

In the initial screen, we genotyped 190 patients and 190 controls (Supplementary Material, Table S1). To avoid false negatives, we set the α-value at 0.05 in the first screen. From 268 SNPs, 22 SNPs in 16 genes showed association with PD ($P < 0.05$) in genotype frequency, allele frequency, dominant model or recessive model. We genotyped the 22 qualifying SNPs in a replication panel of 692 patients and 748 controls and tested again for association. This independent test revealed that SNP0070 (rs7684318 C/T) was prominently associated with PD ($P = 5.0 \times 10^{-10}$ for allele frequency) (Table 1). We corrected the α-value to 0.00019 after Bonferroni's correction (tests for 268 SNPs). The remaining 21 SNPs did not show P-values lower than 0.00019 (data not shown). SNP0070 is located in intron 4 of the *α-synuclein* (*SNCA*) gene on chromosome 4q21. SNCA is a primary component of intracellular inclusions called Lewy bodies, which are considered to be the pathological hallmark of PD (20). Aggregation of SNCA is thought to play a crucial role in the pathogenesis of PD (21). The allele C frequency of SNP0070 was higher in PD (0.67) than in controls (0.57) (Table 1). The association of SNP0070 was significant in genotype frequency, allele frequency, dominant model and recessive model. Of the two disease models, allele C of SNP0070 was more significantly associated in the recessive model than in the dominant model (Table 1).

Linkage disequilibrium (LD) mapping and search for susceptibility SNPs

We performed LD mapping in a 430 kb region around SNP0070. This region contains two genes: *SNCA* and *MMRN1*. Using SNP0070 and 28 additional SNPs in this region, we genotyped 134 control subjects and constructed an LD map based on pairwise D' and r^2 (Fig. 1) (Supplementary Material, Table S2). Three LD blocks were observed on the basis of D' ($D' > 0.9$). The entire *SNCA* gene was included in a block containing SNP0070 (block 2). The *MMRN1* gene was in another LD block, indicating that *MMRN1* does not correlate with the SNP0070 association (Fig. 2).

To search for the most strongly associated SNP(s) in the region, we next performed association studies with these 29 SNPs (Fig. 2; Table 2). We found significant associations for SNPs in block 2, but not in blocks 1 and 3. Block 2, thought to be a susceptibility block for PD, was further analyzed on the basis of r^2-values. Of the 19 SNPs in block 2, 16 belonged to three groups with high pairwise r^2 (>0.85) and the remaining three did not belong to any group (Fig. 1; Table 2) (Supplementary Material, Table S2). Six SNPs in group 1, including originally screened SNP0070 and five additional SNPs (0203, 0204, 0205, 0207 and 0209), showed prominent association with PD ($P = 2.0 \times 10^{-9}$–1.7×10^{-11}, allele 1 versus allele 2) (Fig. 2; Table 2). Population attributable risk (PAR) (22) of SNP0070 was 42.5% in the dominant model and 18.5% in the recessive model.

We next performed haplotype analysis using six representative SNPs in block 2 (Table 3). Six common haplotypes (>1% of PD and controls) covered >90% of the population haplotypes in both PD and controls. The major haplotypes 1 and 2 showed significant associations; however, their P-values were not lower than that of any single SNP in group 1. Therefore, the presence of hidden SNP(s) with a lower P-value than group 1 seemed unlikely, as was the possibility that the haplotype(s) is implicated in PD susceptibility. These findings establish the six SNPs in group 1 as the strongest susceptibility SNPs. All showed stronger associations in the recessive model than in the dominant model, similar to the originally screened SNP0070 (Table 4).

Taken together, our genetic analyses indicate that *SNCA* is a definite susceptibility gene for sporadic PD and that multiple SNPs in group 1 are susceptibility SNPs, likely in a recessive model.

Table 1. Association of SNP0070 in *SNCA* between cases and controls

	Genotype				Allele			*P*-value (χ^2-test)			
	CC	CT	TT	Total	C	T	Total	Genotype	Allele	Dominant[a] model	Recessive[b] model
First screen											
Case	87 (0.46)	87 (0.46)	14 (0.07)	188	261 (0.69)	115 (0.31)	376	3.4×10^{-4}	1.8×10^{-4}	1.8×10^{-4}	1.1×10^{-2}
Control	62 (0.33)	85 (0.46)	39 (0.21)	186	209 (0.56)	163 (0.44)	372				
Replication											
Case	298 (0.44)	307 (0.45)	75 (0.11)	680	903 (0.66)	457 (0.34)	1360	1.3×10^{-6}	4.2×10^{-7}	1.5×10^{-3}	9.0×10^{-7}
Control	233 (0.31)	387 (0.52)	126 (0.17)	746	853 (0.57)	639 (0.43)	1492				
Total											
Case	385 (0.44)	394 (0.45)	89 (0.10)	868	1164 (0.67)	572 (0.33)	1736	2.7×10^{-9}	5.0×10^{-10}	5.7×10^{-6}	2.8×10^{-8}
Control	295 (0.32)	472 (0.51)	165 (0.18)	932	1062 (0.57)	802 (0.43)	1864				

Frequencies of genotypes and alleles are in parentheses.
[a]Genotype CC+CT versus TT.
[b]Genotype CC versus CT+TT.

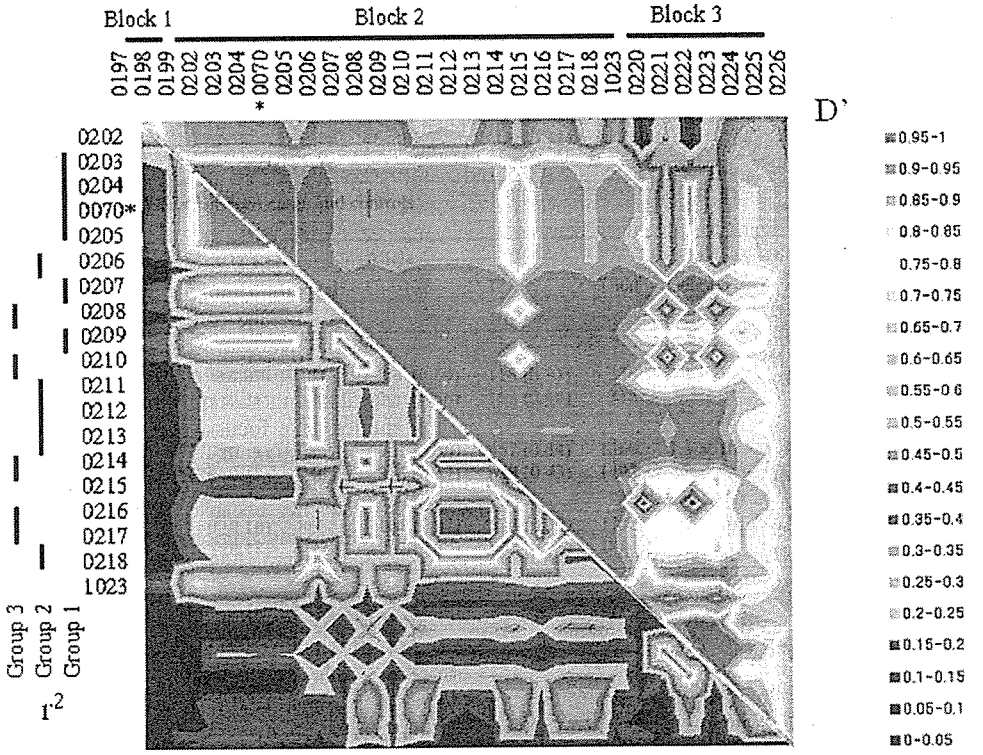

Figure 1. LD structure of the susceptibility region for sporadic PD. Pairwise LD between SNPs, as measured by D' in 134 controls, is graphically indicated. The region spanning 430 kb around the originally screened SNP0070(*) was divided into three LD blocks ($D' > 0.9$) (upper right). On the basis of r^2, SNPs in block 2, including SNP0070, were further divided into three groups ($r^2 > 0.85$) and three solitary SNPs (lower left). The scale is nominal.

SNCA gene expression in relation to susceptibility genotypes

To examine whether the strongest associated SNPs (group 1) affect *SNCA* gene expression, we further quantified *SNCA* mRNA in autopsied frontal cortices and compared the values among the genotypes. SNP0070, in which allele C is associated with PD, was used as a representative of group 1.

The relative values of *SNCA* mRNA for all cases ($n = 21$) and all controls ($n = 18$) were 1.07 ± 0.10 and 0.95 ± 0.13, respectively, showing almost the same level ($P = 0.46$, Student's t-test). When compared among the genotypes in cases, the mean tended to decrease in the order of CC, CT and TT (Fig. 3), although the differences did not reach the significant levels ($P = 0.71$ for CC versus CT, $P = 0.16$ for CT versus TT and $P = 0.32$ for CC versus TT). Similar tendency

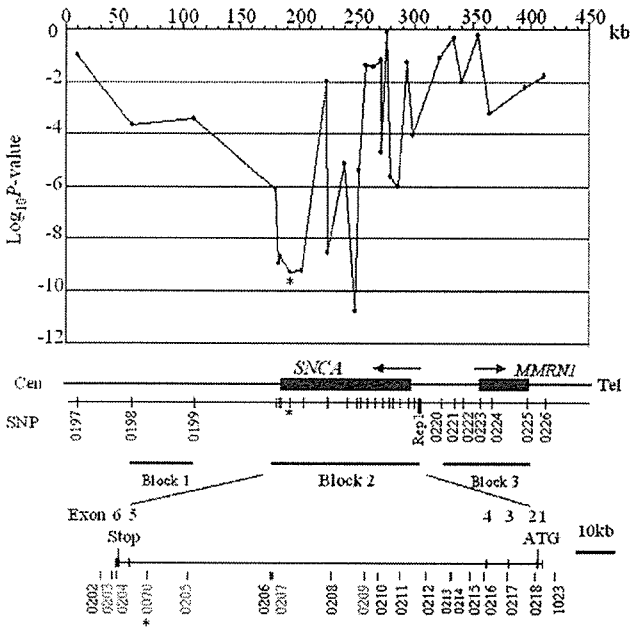

Figure 2. Genomic structure and SNPs of the susceptibility region for sporadic PD and case–control association studies (882 cases and 938 controls). Log *P*-values (allele 1 versus allele 2) are plotted against the physical location of the SNPs. The region includes two genes: *SNCA* and *MMRN1*; transcription orientation is indicated by horizontal arrows. Physical locations of SNPs are shown as axial bars with our experimental ID number. The originally screened SNP0070 is indicated by an asterisk. The location of Rep1, a well-known repeat polymorphism in the *SNCA* promoter region, is indicated by a thick bar. SNPs in block 2 are nominated in an expanded map with the exon–intron structure of *SNCA*. SNPs in group 1 are shown in red. Note that *P*-values are prominently low at the group 1 SNPs located in the 3′ region of *SNCA*. *P*-values in the region around Rep1 are far from significant when compared with those in group 1.

was observed in controls. The mean tended to decrease in the order of CC, CT and TT (Fig. 3) ($P = 0.33$ for CC versus CT, $P = 0.59$ for CT versus TT and $P = 0.54$ for CC versus TT).

These results indicate the possibility that expression of *SNCA* mRNA in the brain tends to be positively correlated with the number of PD-associated allele.

DISCUSSION

To identify susceptibility genes for PD, we performed an extensive candidate gene approach by screening 268 SNPs in 121 genes and identified a prominent association with SNP0070 (rs7684318) in the *SNCA* gene (Table 1). LD mapping localized the entire *SNCA* gene within a single LD block (Figs 1 and 2). Within this block, six SNPs including SNP0070 were in a tight LD group and most strongly associated with PD (Fig. 2; Table 2). The major allele of each SNP in group 1 was positively associated with PD, more strongly in the recessive model than in the dominant model (Table 4). Our genetic analyses establish *SNCA* as a definite susceptibility gene for PD and identify multiple SNPs in group 1 as susceptibility SNPs. Recently, Mueller *et al.* (23) reported that multiple regions of *SNCA* are associated with PD in the German population. Associated SNPs identified by Mueller *et al.* included rs356165 ($P = 1.5 \times 10^{-4}$), which corresponds to SNP0204 in our study, indicating that this SNP has a similar association in Caucasians. Pals *et al.* (24) previously reported no association of the haplotype containing rs356165 with PD in Belgian samples. This contradictory finding may be, at least in part, due to a small sample size (175 cases and 186 controls), as mentioned by the authors.

SNCA/α-synuclein was originally identified in the electric organ of the Pacific electric ray (25). SNCA is a presynaptic protein that is highly and broadly expressed in the brain, but its normal function remains unknown (21). It is a major component of Lewy bodies, the pathological hallmark of PD (20), and the aggregation of SNCA protein is thought to play a crucial role in the loss of dopaminergic neurons (21,26).

SNCA was also the first gene identified as a causative gene in familial PD. Three missense mutations in *SNCA* were reported in families with AD inheritance (6,27,28). These mutations are thought to increase the aggregation of SNCA protein. Point mutations in *SNCA* have not been identified in sporadic PD (27,29), and no SNPs have been found in the coding region, suggesting that disease-related amino acid changes in SNCA are unlikely in sporadic PD.

Genes' overdosage is a potential mechanism for the influence of *SNCA* in PD. Triplication of the *SNCA* locus has been seen in an AD PD family (30), and doubling of *SNCA* gene dosage by triplication has been shown to result in the doubling of mRNA and protein expression in blood and brain (31). Duplication of *SNCA* has also been identified as a cause of familial PD (32,33). Clinical features of patients with *SNCA* duplication resemble those of sporadic cases and are much milder than those with triplication. Taken together, these observations indicate a correlation between increased SNCA protein levels and disease risk. Identification of one or more polymorphisms related to *SNCA* expression level might reveal strong susceptibility indicators for sporadic PD. Many studies have focussed on a mixed repeat microsatellite polymorphism called Rep1 (34), because of its location in the *SNCA* promoter region. However, their significance is uncertain, possibly because of the small number of samples (35–37). Our study demonstrates that the *P*-values of SNPs around Rep1 (0218, 1023 and 0220) are less significant than that of the SNPs in group 1 (Fig. 2). In addition, we genotyped our samples for Rep1. Pairwise *D′*-values showed that Rep1 was not in block 2, but on the boundary (Supplementary Material, Table S2). *P*-value of Rep1 was 7.5×10^{-7} (Supplementary Material, Table S3), which might be explained by its intermediate correlation with the strongest susceptibility SNPs (group 1, $P = 2.0 \times 10^{-9}$–1.7×10^{-11}). Our findings suggest that *P*-value of Rep1 depends on its LD strength with SNPs in group 1. LD strength may be modified by the unstableness of microsatellite markers (38) and may vary among races (39). Taken together, these findings may also partly explain the contradictory findings of previous Rep1 association studies.

To investigate the relationship between the SNPs in group 1 and the *SNCA* expression levels, we analyzed *SNCA* mRNA expression in autopsied frontal cortices (Fig. 3). *SNCA* expression levels tended to be positively correlated with the number of the PD-associated allele, supporting the popular hypothesis that increased SNCA leads to the disease.

Table 2. Association analysis in *SNCA* and surrounding region

SNPs			LD block	Genotype							
	Alleles			Case		Control		MAF	Allele 1 versus allele 2		HWE
ID (rs ID)	12	Location	(group)	11/12/22	(Total)	11/12/22	(Total)	Case/control	*P*-value	OR (95% CI)	Case/control
0197 (rs3733450)	TC		1	38/286/549	(873)	33/280/619	(932)	0.21/0.19	0.10	1.15 (0.97–1.36)	1.00/0.93
0198 (rs1390280)	AG		1	366/384/118	(868)	316/454/162	(932)	0.36/0.42	2.1×10^{-4}	1.29 (1.13–1.46)	0.32/1.00
0199 (rs3733449)	CT		1	117/375/374	(866)	154/451/322	(927)	0.35/0.41	3.7×10^{-4}	1.28 (1.11–1.48)	0.16/0.91
0202 (rs356221)	TA	3′-flanking	2	73/369/431	(873)	123/449/360	(932)	0.30/0.37	7.2×10^{-7}	1.42 (1.25–1.63)	0.69/0.40
0203 (rs3857053)	TC	3′-flanking	2 (1)	380/406/87	(873)	293/476/164	(933)	0.33/0.43	1.1×10^{-9}	1.53 (1.33–1.73)	0.18/0.24
0204 (rs356165)	GA	3′-UTR	2 (1)	379/399/89	(867)	289/482/159	(930)	0.33/0.43	2.0×10^{-9}	1.52 (1.33–1.74)	0.32/0.09
0070[a] (rs7684318)	CT	Intron 4	2 (1)	385/394/89	(868)	295/472/165	(932)	0.33/0.43	5.0×10^{-10}	1.54 (1.35–1.75)	0.47/0.35
0205 (rs3775424)	CT	Intron 4	2 (1)	87/406/376	(869)	166/477/288	(931)	0.33/0.43	5.4×10^{-10}	1.52 (1.34–1.75)	0.16/0.22
0206 (rs3775426)	CT	Intron 4	2 (2)	56/350/456	(862)	53/324/555	(932)	0.27/0.23	0.0098	1.22 (1.05–1.41)	0.35/0.59
0207 (rs3796661)	CT	Intron 4	2 (1)	91/367/382	(840)	154/482/296	(932)	0.33/0.42	2.7×10^{-9}	1.52 (1.31–1.76)	0.90/0.08
0208 (rs3775435)	GA	Intron 4	2 (3)	157/434/272	(863)	115/439/375	(929)	0.43/0.36	7.3×10^{-6}	1.36 (1.18–1.56)	0.53/0.48
0209 (rs2737029)	TC	Intron 4	2 (1)	84/377/402	(863)	156/480/297	(933)	0.32/0.42	1.7×10^{-11}	1.60 (1.40–1.83)	0.81/0.12
0210 (rs3775442)	TC	Intron 4	2 (3)	158/438/274	(870)	114/440/378	(932)	0.43/0.36	4.2×10^{-6}	1.37 (1.19–1.58)	0.50/0.46
0211 (rs3756055)	GA	Intron 4	2 (2)	50/339/481	(870)	49/319/565	(933)	0.25/0.22	0.042	1.17 (1.00–1.37)	0.38/0.72
0212 (rs3775446)	TG	Intron 4	2 (2)	50/340/480	(870)	49/317/565	(931)	0.25/0.22	0.034	1.19 (1.01–1.38)	0.36/0.67
0213 (rs3756056)	CT	Intron 4	2 (2)	50/340/482	(872)	48/323/557	(928)	0.25/0.23	0.062	1.16 (0.99–1.34)	0.37/0.97
0214 (rs894278)	GT	Intron 4	2 (3)	156/438/275	(869)	117/441/375	(933)	0.43/0.36	1.9×10^{-5}	1.34 (1.18–1.52)	0.46/0.52
0215 (rs1812923)	CA	Intron 4	2	74/383/413	(870)	92/392/447	(931)	0.31/0.31	0.79	1.01 (0.89–1.16)	0.30/0.71
0216 (rs2298728)	AG	Intron 4	2 (3)	163/432/274	(869)	117/435/380	(932)	0.44/0.36	2.2×10^{-6}	1.38 (1.22–1.56)	0.80/0.72
0217 (rs3796667)	AT	Intron 3	2 (3)	159/430/271	(860)	114/428/383	(925)	0.44/0.36	9.2×10^{-7}	1.41 (1.23–1.61)	0.66/0.80
0218 (rs2035268)	TG	Intron 2	2 (2)	475/339/54	(868)	556/326/51	(933)	0.26/0.23	0.049	1.16 (0.99–1.37)	0.59/0.79
1023 (rs1023777)	CT	5′-flanking	2	66/318/464	(848)	86/433/411	(930)	0.27/0.33	9.3×10^{-5}	1.33 (1.15–1.55)	0.31/0.08
0220 (rs2736994)	GA		3	542/263/22	(827)	529/292/33	(854)	0.19/0.21	0.081	1.16 (0.98–1.38)	0.17/0.41
0221 (rs11097239)	CA		3	245/437/182	(864)	272/431/226	(929)	0.46/0.48	0.48	1.05 (0.92–1.19)	0.67/0.04
0222 (rs1899389)	AG		3	592/245/29	(866)	586/297/46	(929)	0.18/0.21	0.009	1.25 (1.05–1.46)	0.64/0.34
0223 (rs2289515)	AT		3	180/436/238	(854)	221/423/267	(911)	0.47/0.48	0.6	1.03 (0.90–1.18)	0.49/0.04
0224 (rs3775464)	GA		3	109/414/346	(869)	95/385/449	(929)	0.36/0.31	5.9×10^{-4}	1.28 (1.11–1.46)	0.43/0.40
0225 (rs1246270)	GA		3	372/394/84	(850)	474/372/81	(927)	0.33/0.29	0.0061	1.21 (1.05–1.40)	0.19/0.56
0226 (rs3822098)	CT		3	50/300/514	(864)	59/376/494	(929)	0.23/0.27	0.017	1.21 (1.04–1.40)	0.54/0.30

MAF, minor allele frequency. When the odds ratio (OR) is less than 1, an inverted score is indicated.
[a]Originally screened SNP.

Table 3. Haplotype association analysis using representative SNPs in block 2

Haplotypes	Representative SNP (group)						Haplotype frequency		*P*-value
	202	0070 (1)	0206 (2)	0214 (3)	0215	1023	Case	Control	
1	A	C	T	G	A	T	0.39	0.33	4.4×10^{-5}
2	T	T	T	T	A	C	0.24	0.3	5.0×10^{-6}
3	A	C	C	T	C	T	0.24	0.21	0.071
4	A	T	T	T	C	T	0.03	0.06	3.3×10^{-4}
5	T	T	T	T	C	T	0.02	0.03	0.083
6	T	T	T	G	A	T	0.01	0.02	0.62

Table 4. Association of the SNPs in group 1 of block 2

SNP	Allele	Genotype						Dominant model (MM + Mm versus mm)		Recessive model (MM versus Mm + mm)	
		Case			Control						
	M/m	MM	Mm	mm	MM	Mm	mm	*P*-value	Odds ratio (95% CI)	*P*-value	Odds ratio (95%CI)
0203	T/C	380	406	87	293	476	164	3.0×10^{-6}	1.95 (1.45–2.52)	1.0×10^{-7}	1.68 (1.41–2.07)
0204	G/A	379	399	89	289	482	159	2.7×10^{-5}	1.81 (1.36–2.38)	3.0×10^{-8}	1.72 (1.43–2.13)
0070[a]	C/T	385	394	89	295	472	165	5.7×10^{-6}	1.90 (1.44–2.53)	2.8×10^{-8}	1.71 (1.42–2.06)
0205	T/C	376	406	87	288	477	166	1.8×10^{-6}	1.98 (1.45–2.61)	6.0×10^{-8}	1.69 (1.40–2.05)
0207	T/C	382	367	91	296	482	154	5.3×10^{-4}	1.66 (1.25–2.16)	3.0×10^{-9}	1.78 (1.47–2.16)
0209	C/T	402	377	84	297	480	156	1.4×10^{-5}	1.89 (1.41–2.51)	1.5×10^{-10}	1.86 (1.55–2.27)

M and m are major allele and minor allele, respectively. CI, confidence interval.
[a]Originally screened SNP.

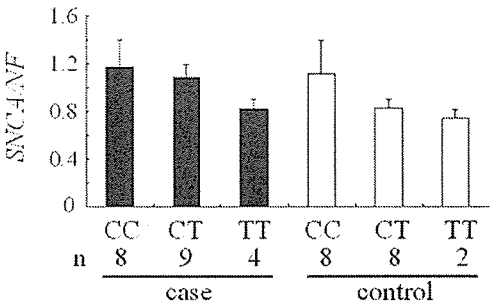

Figure 3. *In vivo* expression of *SNCA* mRNA in relation to susceptibility genotypes. SNP0070 (C/T) is used as a representative of group 1. *SNCA* expression levels in autopsied frontal cortices of cases (solid bar; 8 CC, 9 CT and 4 TT) and controls (open bar; 8 CC, 8 CT and 2 TT). Relative *SNCA* mRNA levels (normalized to *neurofilament L, NF*) are indicated. In cases, mean ± SEM of CC, CT and TT were 1.17 ± 0.23, 1.08 ± 0.11 and 0.82 ± 0.08, respectively. In controls, mean ± SEM of CC, CT and TT were 1.11 ± 0.28, 0.83 ± 0.07 and 0.75 ± 0.07, respectively.

The PD-associated alleles may positively correlate with the basal transcription level of *SNCA* and/or the induction of *SNCA* expression by certain stimulators, for example, oxidative stress.

Other possible functional effects of associated SNPs include alternative splicing, which may result in a protein isoform that aggregates more readily. The C-terminal region of SNCA is rich in acidic amino acid residues, and its truncation promotes aggregation *in vitro* (40,41). The known splice variant *SNCA112* lacks exon 5, which encodes 28 amino acids (10 of which are acidic) in frame. Thus, SNCA112 may also promote aggregation. We investigated *SNCA112* mRNA expression in frontal cortices using splice variant-specific primers, but observed little difference among the three genotypes (data not shown).

In summary, our study establishes *SNCA* as a susceptibility gene for sporadic PD. Focussed investigations of SNCA function will further enhance our understanding of how genetic factors contribute to the complex etiology of PD.

MATERIALS AND METHODS

Subjects

We recruited 882 unrelated sporadic PD patients (age, 64.9 ± 9.8; male/female ratio, 0.79) and 938 unrelated controls (age, 45.3 ± 16.3; male/female ratio, 1.10). The diagnosis of idiopathic PD was based on the presence of two or more of the cardinal features of PD (tremor, rigidity, bradykinesia and postural instability), according to the criteria for sporadic PD (42). Patients were evaluated by the certified neurologists specializing in PD. The average age of onset was 57.4 ± 10.9 years. Forty-two patients showed early onset of PD (<40 years) and 51 patients had a positive family history of PD. Patients who carried *parkin* mutations were excluded. All patients and controls were of Japanese ancestry. Informed consent was obtained from each individual, and approval for the study was obtained from the University Ethical Committees.

SNP genotyping

Genomic DNA was extracted from whole blood using FlexGene (Qiagen). SNP information was obtained from the dbSNP (http://www/ncbi.nlm.nih.gov/SNP/), JSNP (http://snp.ims.u-tokyo.ac.jp/) (43) and Celera Discovery System

(http://myscience.appliedbiosystems.com/) databases. We genotyped SNPs using the Invader assay (Third Wave Technologies), TaqMan (Applied Biosystems) or direct sequencing using an ABI3730 capillary sequencer (Applied Biosystems). Rep1 genotyping and allele designations followed those described previously (35). The Rep1 region was amplified using FAM5′-CCTGGCATATTTGATTGCAA-3′ and 5′-GACTGGCCCAAGATTAACCA-3′ as primers and analyzed using ABI3730 capillary sequencer.

Statistical analysis

SNPAlyze software (DYNACOM, Japan) was used for the case–control study (χ^2-test), calculation of odds ratio and its 95% CI (Bootstrap method), haplotype analysis (Expectation–Maximization algorithm) and pairwise LD analysis (Lewontin's coefficient D' and standardized coefficient r).

Real-time RT–PCR

Autopsied frontal cortices were obtained from the Brain Bank for Aging Research (Tokyo Metropolitan Geriatric Hospital/Tokyo Metropolitan Institute of Gerontology) and from the Department of Neurology, Juntendo University School of Medicine. The samples contained 21 cases [age, 82.6 ± 7.1 (SD) years; 11 males and 10 females] with Lewy body pathology defined by the third Consensus Guideline for Dementia with Lewy Bodies (44), comprising PD with and without dementia and dementia with Lewy bodies, and 18 control subjects (age, 81.2 ± 5.2; 12 males and six females) without parkinsonism or dementia and without neurodegenerative pathological changes. Total RNA was extracted from tissues using RNeasy (Qiagen), and cDNA was prepared using Superscript reverse transcriptase (Invitrogen). Real-time RT–PCR was carried out on ABI PRISM 7900 sequence detection system (Applied Biosystems) using SYBR Premix Ex Taq (TAKARA, Japan). First-strand cDNA was amplified using primers specific for *SNCA* (forward: 5′-GCAGAAGCA GCAGGAAAGAC-3′; reverse: 5′-CTGGGCTACTGCTGTC ACAC-3′; product size: 159 bp) and *NF* (*neurofilament L*, forward: 5′-AGAACGCTGAGGAATGGTTC-3′; reverse: 5′-CTGGTGAAACTGAGTCGGGT-3′; product size: 391 bp). A single band of the expected size was amplified from cDNA samples, but not from RNA samples. For quantification, we used a relative standard curve method. Standard curves of *SNCA* and *NF* were generated from the amplification of diluted series of cDNA from cortices. *SNCA* expression levels were normalized to those of *NF*. One of the experimental samples was used as the calibrator. Each of the normalized *SNCA* values was divided by the calibrator normalized *SNCA* value to generate the relative expression levels. The values were determined in triplicate. Reproducibility of the results was confirmed by repeating cDNA synthesis and real-time PCR twice for seven samples, and similar results were obtained.

SUPPLEMENTARY MATERIAL

Supplementary Material is available at HMG Online.

ACKNOWLEDGEMENTS

We thank PD patients for participating in the study. We also thank Dr Ryo Yamada for graphical LD analysis; Drs Jun Ohashi, Toshihiro Tanaka and Shiro Ikegawa for helpful comments; Mio Yoshida, Drs Helena A. Popiel, Yushi Hirota and Katsushi Tokunaga for help of performing the study and Dr Jennifer Logan for editing the manuscript. This work was supported by the 21st Century COE program and Research Grant (14013037 and 17590874), both from the Ministry of Education, Culture, Sports, Science and Technology of Japan; by the Research Grant for Nervous and Mental Disorders (14B-3) and Grant for Research on Measures for Intractable Diseases (H14-Q-15-1), both from the Ministry of Health, Labor and Welfare of Japan and by a grant from Core Research for Evolutional Science and Technology (CREST) of the Japan Science and Technology Agency (JST).

Conflict of Interest statement. None declared.

REFERENCES

1. Rascol, O., Payoux, P., Ory, F., Ferreira, J.J., Brefel-Courbon, C. and Montastruc, J.-L. (2003) Limitations of current Parkinson's disease therapy. *Ann. Neurol.*, **53** (Suppl. 3), S3–S12.
2. Warner, T.T. and Schapira, A.H. (2003) Genetic and environmental factors in the cause of Parkinson's disease. *Ann. Neurol.*, **53** (Suppl. 3), S16–S23.
3. Elbaz, A., Grigoletto, F., Baldereschi, M., Breteler, M.M., Manubens-Bertran, J.M., Lopez-Pousa, S., Dartigues, J.F., Alperovitch, A., Tzourio, C., Rocca, W.A. *et al.* (1999) Familial aggregation of Parkinson's disease: a population-based case–control study in Europe. *Neurology*, **52**, 1876–1882.
4. Sveinbjörnsdóttir, S., Hicks, A.A., Jónsson, T., Pétursson, H., Gugmundsson, G., Frigge, M.L., Kong, A., Gulcher, J.R. and Stefánsson, K. (2000) Familial aggregation of Parkinson's disease in Iceland. *N. Engl. J. Med.*, **343**, 1765–1770.
5. Piccini, P., Burn, D.J., Ceravolo, R., Maraganore, D. and Brooks, D.J. (1999) The role of inheritance in sporadic Parkinson's disease: evidence from a longitudinal study of dopaminergic function in twins. *Ann. Neurol.*, **45**, 577–582.
6. Polymeropoulos, M.H., Lavedan, C., Leroy, E., Ide, S.E., Dehejia, A., Dutra, A., Pike, B., Root, H., Rubenstein, J., Boyer, R. *et al.* (1997) Mutation in the α-synuclein gene identified in families with Parkinson's disease. *Science*, **276**, 2045–2047.
7. Kitada, T., Asakawa, S., Hattori, N., Matsumine, H., Yamamura, Y., Minoshima, S., Yokochi, M., Mizuno, Y. and Shimizu, N. (1998) Mutations in the *parkin* gene cause autosomal recessive juvenile parkinsonism. *Nature*, **392**, 605–608.
8. Leroy, E., Boyer, R., Auburger, G., Leube, B., Ulm, G., Mezey, E., Harta, G., Brownstein, M.J., Jonnalagada, S., Chernova, T. *et al.* (1998) The ubiquitin pathway in Parkinson's disease. *Nature*, **395**, 451–452.
9. Valente, E.M., Abou-Sleiman, P.M., Caputo, V., Muqit, M.M.K., Harvey, K., Gispert, S., Ali, Z., Del Turco, D., Bentivoglio, A.R., Healy, D.G. *et al.* (2004) Hereditary early-onset Parkinson's disease caused by mutations in *PINK1*. *Science*, **304**, 1158–1160.
10. Bonifati, V., Rizzu, P., van Baren, M.J., Schaap, O., Breedveld, G.J., Krieger, E., Dekker, M.C.J., Squitieri, F., Ibanez, P., Joosse, M. *et al.* (2003) Mutations in the *DJ-1* gene associated with autosomal recessive early-onset parkinsonism. *Science*, **299**, 256–259.
11. Paisán-Ruiz, C., Jain, S., Evans, E.W., Gilks, W.P., Simón, J., van der Brug, M., Lopez de Munain, A., Aparicio, S., Gil, A.M., Khan, N. *et al.* (2004) Cloning of the gene containing mutations that cause *PARK8*-linked Parkinson's disease. *Neuron*, **44**, 595–600.
12. Zimprich, A., Biskup, S., Leitner, P., Lichtner, P., Farrer, M., Lincoln, S., Kachergus, J., Hulihan, M., Uitti, R.J., Calne, D.B. *et al.* (2004) Mutations in *LRRK2* cause autosomal-dominant parkinsonism with pleomorphic pathology. *Neuron*, **44**, 601–607.

13. Le, W.-D., Xu, P., Jankovic, J., Jiang, H., Appel, S.H., Smith, R.G. and Vassilatis, D.K. (2003) Mutations in *NR4A2* associated with familial Parkinson disease. *Nat. Genet.*, **33**, 85–89.
14. DeStefano, A.L., Golbe, L.I., Mark, M.H., Lazzarini, A.M., Maher, N.E., Saint-Hilaire, M., Feldman, R.G., Guttman, M., Watts, R.L., Suchowersky, O. *et al.* (2001) Genome-wide scan for Parkinson's disease: the *Gene*PD Study. *Neurology*, **57**, 1124–1126.
15. Hicks, A.A., Pétursson, H., Jónsson, T., Stefánsson, H., Jóhannsdóttir, H.S., Sainz, J., Frigge, M.L., Kong, A., Gulcher, J.R., Stefánsson, K. *et al.* (2002) A susceptibility gene for late-onset idiopathic Parkinson's disease. *Ann. Neurol.*, **52**, 549–555.
16. Pankratz, N., Nichols, W.C., Uniacke, S.K., Halter, C., Rudolph, A., Shults, C., Conneally, P.M., Foroud, T. and the Parkinson Study Group (2002) Genome screen to identify susceptibility genes for Parkinson disease in a sample without *parkin* mutations. *Am. J. Hum. Genet.*, **71**, 124–135.
17. Scott, W.K., Nance, M.A., Watts, R.L., Hubble, J.P., Koller, W.C., Lyons, K., Pahwa, R., Stern, M.B., Colcher, A., Hiner, B.C. *et al.* (2001) Complete genomic screen in Parkinson disease: evidence for multiple genes. *JAMA*, **286**, 2239–2244.
18. Martin, E.R., Scott, W.K., Nance, M.A., Watts, R.L., Hubble, J.P., Koller, W.C., Lyons, K., Pahwa, R., Stern, M.B., Colcher, A. *et al.* (2001) Association of single-nucleotide polymorphisms of the tau gene with late-onset Parkinson disease. *JAMA*, **286**, 2245–2250.
19. van der Walt, J.M., Noureddine, M.A., Kittappa, R., Hauser, M.A., Scott, W.K., McKay, R., Zhang, F., Stajich, J.M., Fujiwara, K., Scott, B.L. *et al.* (2004) Fibroblast growth factor 20 polymorphisms and haplotypes strongly influence risk of Parkinson disease. *Am. J. Hum. Genet.*, **74**, 1121–1127.
20. Spillantini, M.G., Schmidt, M.L., Lee, V.M.-Y., Trojanowski, J.Q., Jakes, R. and Goedert, M. (1997) α-synuclein in Lewy bodies. *Nature*, **388**, 839–840.
21. Goedert, M. (2001) Alpha-synuclein and neurodegenerative diseases. *Nat. Rev. Neurosci.*, **2**, 492–501.
22. Schildkraut, J.M. (1998) Examining complex genetic interactions. In Haines, J.L. and Pericak-Vance, M.A. (eds), *Approaches to Gene Mapping in Complex Human Diseases*. Wiley-Liss, NY, pp. 379–410.
23. Mueller, J.C., Fuchs, J., Hofer, A., Zimprich, A., Lichtner, P., Illig, T., Berg, D., Wüllner, U., Meitinger, T. and Gasser, T. (2005) Multiple regions of α-synuclein are associated with Parkinson's disease. *Ann. Neurol.*, **57**, 535–541.
24. Pals, P., Lincoln, S., Manning, J., Heckman, M., Skipper, L., Hulihan, M., Van den Broeck, M., De Pooter, T., Cras, P., Crook, J. *et al.* (2004) α-Synuclein promoter confers susceptibility to Parkinson's disease. *Ann. Neurol.*, **56**, 591–595.
25. Maroteaux, L., Campanelli, J.T. and Scheller, R.H. (1988) Synuclein: a neuron-specific protein localized to the nucleus and presynaptic nerve terminal. *J. Neurosci.*, **8**, 2804–2815.
26. Eriksen, J.L., Dawson, T.M., Dickson, D.W. and Petrucelli, L. (2003) Caught in the act: α-synuclein is the culprit in Parkinson's disease. *Neuron*, **40**, 453–456.
27. Krüger, R., Kuhn, W., Müller, T., Woitalla, D., Graeber, M., Kösel, S., Przuntek, H., Epplen, J.T., Schöls, L. and Riess, O. (1998) Ala30Pro mutation in the gene encoding α-synuclein in Parkinson's disease. *Nat. Genet.*, **18**, 106–108.
28. Zarranz, J.J., Alegre, J., Gómez-Esteban, J.C., Lezcano, E., Ros, R., Ampuero, I., Vidal, L., Hoenicka, J., Rodriguez, O., Atarés, B. *et al.* (2004) The new mutation, E46K, of α-synuclein causes Parkinson and Lewy body dementia. *Ann. Neurol.*, **55**, 164–173.
29. Nagar, S., Juyal, R.C., Chaudhary, S., Behari, M., Gupta, M., Rao, S.N. and Thelma, B.K. (2001) Mutations in the α-synuclein gene in Parkinson's disease among Indians. *Acta Neurol. Scand.*, **103**, 120–122.
30. Singleton, A.B., Farrer, M., Johnson, J., Singleton, A., Hague, S., Kachergus, J., Hulihan, M., Peuralinna, T., Dutra, A., Nussbaum, R. *et al.* (2003) α-Synuclein locus triplication causes Parkinson's disease. *Science*, **302**, 841.
31. Miller, D.W., Hague, S.M., Clarimon, J., Baptista, M., Gwinn-Hardy, K., Cookson, M.R. and Singleton, A.B. (2004) α-synuclein in blood and brain from familial Parkinson disease with *SNCA* locus triplication. *Neurology*, **62**, 1835–1838.
32. Chartier-Harlin, M.-C., Kachergus, J., Roumier, C., Mouroux, V., Douay, X., Lincoln, S., Levecque, C., Larvor, L., Andrieux, J., Hulihan, M. *et al.* (2004) α-synuclein locus duplication as a cause of familial Parkinson's disease. *Lancet*, **364**, 1167–1169.
33. Ibáñez, P., Bonnet, A.-M., Débarges, B., Lohmann, E., Tison, F., Pollak, P., Agid, Y., Dürr, A., Brice, A. and French Parkinson's Disease Genetics Study Group (2004) Causal relation between α-synuclein gene duplication and familial Parkinson's disease. *Lancet*, **364**, 1169–1171.
34. Xia, Y., Rohan de Silva, H.A., Rosi, B.L., Yamaoka, L.H., Rimmler, J.B., Pericak-Vance, M.A., Roses, A.D., Chen, X., Masliah, E., DeTeresa, R. *et al.* (1996) Genetic studies in Alzheimer's disease with an NACP/α-synuclein polymorphism. *Ann. Neurol.*, **40**, 207–215.
35. Farrer, M., Maraganore, D.M., Lockhart, P., Singleton, A., Lesnick, T.G., de Andrade, M., West, A., de Silva, R., Hardy, J. and Hernandez, D. (2001) α-synuclein gene haplotypes are associated with Parkinson's disease. *Hum. Mol. Genet.*, **10**, 1847–1851.
36. Parsian, A., Racette, B., Zhang, Z.H., Chakraverty, S., Rundle, M., Goate, A. and Perlmutter, J.S. (1998) Mutation, sequence analysis, and association studies of α-synuclein in Parkinson's disease. *Neurology*, **51**, 1757–1759.
37. Tan, E.-K., Tan, C., Shen, H., Chai, A., Lum, S.-Y., Teoh, M.-L., Yih, Y., Wong, M.-C. and Zhao, Y. (2003) Alpha synuclein promoter and risk of Parkinson's disease: microsatellite and allelic size variability. *Neurosci. Lett.*, **336**, 70–72.
38. Jobling, M.A., Hurles, M. and Tyler-Smith, C. (2004) *Human Evolutionary Genetics*. Garland Science, NY, pp. 45–86.
39. Altshuler, D., Brooks, L.D., Chakravarti, A., Collins, F.S., Daly, M.J., Donnelly, P. and the International HapMap Consortium (2005) A haplotype map of the human genome. *Nature*, **437**, 1299–1320.
40. Murray, I.V.J., Giasson, B.I., Quinn, S.M., Koppaka, V., Axelsen, P.H., Ischiropoulos, H., Trojanowski, J.Q. and Lee, V.M.-Y. (2003) Role of α-synuclein carboxy-terminus on fibril formation *in vitro*. *Biochemistry*, **42**, 8530–8540.
41. Serpell, L.C., Berriman, J., Jakes, R., Goedert, M. and Crowther, R.A. (2000) Fiber diffraction of synthetic α-synuclein filaments shows amyloid-like cross-β conformation. *Proc. Natl Acad. Sci. USA*, **97**, 4897–4902.
42. Bower, J.H., Maraganore, D.M., McDonnell, S.K. and Rocca, W.A. (1999) Incidence and distribution of Parkinsonism in Olmsted County, Minnesota, 1976–1990. *Neurology*, **52**, 1214–1220.
43. Haga, H., Yamada, R., Ohnishi, Y., Nakamura, Y. and Tanaka, T. (2002) Gene-based SNP discovery as part of the Japanese Millennium Genome Project: identification of 190 562 genetic variations in the human genome. *J. Hum. Genet.*, **47**, 605–610.
44. McKeith, I.G., Dickson, D.W., Lowe, J., Emre, M., O'Brien, J.T., Feldman, H., Cummings, J., Duda, J.E., Lippa, C., Perry, E.K. *et al.* (2005) Diagnosis and management of dementia with Lewy bodies: third report of the DLB Consortium. *Neurology*, **65**, 1863–1872.

ELSEVIER

NeuroImage

www.elsevier.com/locate/ynimg
NeuroImage 29 (2006) 1203 – 1211

MAP-based kinetic analysis for voxel-by-voxel compartment model estimation: Detailed imaging of the cerebral glucose metabolism using FDG

Yuichi Kimura,[a,*] Mika Naganawa,[c] Jun Yamaguchi,[b] Yuki Takabayashi,[b] Akihiko Uchiyama,[b] Keiichi Oda,[a] Kenji Ishii,[a] and Kiichi Ishiwata [a]

[a]*Positron Medical Center, Tokyo Metropolitan Institute of Gerontology, 1-1, Naka, Itabashi, Tokyo 173-0022, Japan*
[b]*Graduate School of Science and Engineering, Waseda University, 3-4-1, Ohkubo, Shinjyuku, Tokyo 169-8555, Japan*
[c]*Graduate School of Information Science, Nara Institute of Science and Technology, 8916-5, Takayama, Ikoma, Nara 630-0192, Japan*

Received 28 December 2004; revised 25 August 2005; accepted 31 August 2005
Available online 10 October 2005

We propose a novel algorithm for voxel-by-voxel compartment model analysis based on a maximum a posteriori (MAP) algorithm. Voxel-by-voxel compartment model analysis can derive functional images of living tissues, but it suffers from high noise statistics in voxel-based PET data and extended calculation times. We initially set up a feature space of the target radiopharmaceutical composed of a measured plasma time activity curve and a set of compartment model parameters, and measured the noise distribution of the PET data. The dynamic PET data were projected onto the feature space, and then clustered using the Mahalanobis distance. Our method was validated using simulation studies, and compared with ROI-based ordinary kinetic analysis for FDG. The parametric images exhibited an acceptable linear relation with the simulations and the ROI-based results, and the calculation time took about 10 min. We therefore concluded that our proposed MAP-based algorithm is practical.

Keywords: MAP; PET; Parametric image; FDG; Kinetic analysis

Introduction

The aim of this study was to develop a novel approach for voxel-by-voxel compartment model analysis to form parametric images using positron emission tomography (PET) based on a maximum a posteriori (MAP) approach.

PET can provide various functionalities of living tissues in the form of a spatial distribution of an administered radiopharmaceutical. If the details of a physiological function are required, then a history of the radiopharmaceutical concentrations in a tissue (i.e., the tissue time activity curve, or tTAC) is measured using multiple PET scans, and a compartment model analysis is applied to determine the parameters that describe the behavior of the administered drugs in a target organ (Huang and Phelps, 1986). This process is known as kinetic analysis. Furthermore, kinetic analysis in a voxel-by-voxel fashion provides us with images that can be used to determine the activity of specific enzymes or concentrations of neuroreceptors. However, voxel-based kinetic analysis has two major drawbacks. One is the noise level in a voxel-based tTAC, and the second is the large number of voxels involved. The noise level in a voxel-based tTAC leads to an instability in the estimated parameters. The large number of voxels, which can reach up to half a million, leads to extensive calculation times for image formation.

We have proposed a clustering-based algorithm to overcome this situation, in which voxel-based tTACs are categorized based on their kinetics. The algorithm, Clustering Analysis for Kinetics (CAKS), has been reported for a one-tissue-two-compartment model (Kimura et al., 1999), and a two-tissue-three-compartment model (Kimura et al., 2002). In the CAKS approach, the clustering algorithm is a key term. An unsupervised clustering scheme has also been applied (Kimura, 2004).

This paper introduces MAP approach for a kinetics scheme. This is proposed to improve a robustness for noise interference. In the proposed approach, feature surfaces are provided using an a priori knowledge of the kinetics of the administered radiopharmaceutical, and then, the observed data are clustered. Some simulation studies carried out are discussed to determine the details of the proposed algorithm, and to evaluate its reliability. Parametric images of the brain glucose metabolism are discussed using [^{18}F]fluoro-2-deoxy-D-glucose (FDG).

Method

In the proposed method, the estimated kinetic parameters of a voxel-based tTAC are determined based on similarities of shape, when data are compared with noise-free tTACs that are

* Corresponding author. Fax: +81 3 3964 2188.
E-mail address: ukimura@ieee.org (Y. Kimura).
Available online on ScienceDirect (www.sciencedirect.com).

1053-8119/$ - see front matter © 2005 Elsevier Inc. All rights reserved.
doi:10.1016/j.neuroimage.2005.08.046

formed from a set of parameters that lie within a physiologically feasible range. The shape of a noise-free tTAC is projected onto the feature space, and the noise is expressed as a statistical distribution of a feature point in the space.

Measurement of glucose metabolism using PET

FDG is a glucose analog, and it has been used to measure cerebral glucose metabolism using PET in glucose transport from plasma to tissue, in glucose phosphorylation, and to determine the metabolic rate of glucose.

The behavior of FDG is described by Eq. (1) (Huang et al., 1980):

$$C_o(t) = \frac{k_1}{\alpha_2 - \alpha_1}\{(k_3 + k_4 - \alpha_1)e^{-\alpha_1 t} + (\alpha_2 - k_3 - k_4)e^{-\alpha_2 t}\} \otimes C_p(t), \tag{1}$$

where

$$\alpha_1, \alpha_2 = \frac{k_2 + k_3 + k_4 \mp \sqrt{(k_2 + k_3 + k_4)^2 - 4k_2k_4}}{2}, \tag{2}$$

and $C_o(t)$ and $C_p(t)$ denote the concentration of administered FDG in a target tissue and arterial plasma, respectively. $\otimes$ denotes a convolution. Glucose transportation from a capillary to a tissue and the reverse process are described by the terms k_1 and k_2, respectively, and k_3 and k_4 denote the rate of phosphorylation and dephosphorylation of FDG. The term $C_o(t)$ is derived as a dynamic image from the PET data, and $C_p(t)$ is measured via arterial blood sampling. The term k_4 is ignored in our discussion, because we used scan durations of 60 min (Lucignani et al., 1993).

First, $C_o(t)$ was normalized using its integral to reduce the dimensionality by ignoring k_1, because k_1 appears in both the denominator and numerator of Eq. (3) from Eq. (1), and so cancels out.

$$C(t) = \frac{C_o(t)}{\int_0^{T_E} C_o(\tau)d\tau}, \tag{3}$$

where T_E denotes the time of the last frame.

Definition of the feature surface

The shape of $C(t)$ is represented mathematically as a surface in a feature space, in which a shape is represented by a position (Duda et al., 2001). To define a feature space, dynamic PET data are considered as a vector in n-dimensional space:

$$\boldsymbol{C} \equiv [C(t_1),..,C(t_n)]^T \tag{4}$$

where n is the number of frames. In a feature space, Cs are located at different points that have different shapes from each other.

In reality, the location of the noise-free tTACs in a feature space is identified before parameter estimation using the following steps. When the data from a measured plasma time activity curve (pTAC) are inputted into Eq. (1), a set of tTACs is derived by varying k_2 and k_3 in a suitable range based on physiological considerations: either 0.01 or values between 0.02 and 0.40 with a 0.02 step size for k_2, and values between 0.01 and 0.30 with a step size of 0.01 for k_3, where k_1 is fixed to 0.1. Then, all the generated tTACs are composed as a matrix C_A:

$$C_A \equiv [\boldsymbol{C}_1 ... \boldsymbol{C}_M], \tag{5}$$

and the principal components are calculated to generate a feature space.

If the noise-free tTACs are projected onto this space, shown as the C_1–C_4 in Fig. 1, a curved surface on the noise-free tTACs will be drawn, Π in Fig. 1. Note that first only some principal components are used. This approach decreases the dimensionality and simplifies further data analysis. The optimal dimensionality is discussed later in the text.

Parameter estimation

The noise distribution in a feature space, the likelihood for parameter estimation, is evaluated using the following procedure. To obtain the statistical properties of the noise in the measured tTACs, noisy tTACs are mimicked to add the simulated noise to the noise-free tTACs, assuming that a Gaussian distribution exists with a mean equal to that of the measured tTAC and a variance proportional to that of the tTAC (Kimura et al., 2002). This step means that a multidimensional Gaussian was assumed for the noise distribution in the projected tTAC onto the space. These values are used to determine the noise amplitude such that the simulated tTACs have the same noise level as those of the measured voxel-based tTACs.

The semantic diagram is available in Fig. 1. Noise-free tTACs are projected onto a point in the space defined by Eq. (4) (C_1–C_4 in Fig. 1). The noise perturbs the shape of the noise-free tTAC, and causes a fluctuation in the projected point. This fluctuation is assumed to be a multidimensional Gaussian, centered at its noise-free position of C_1–C_4. The covariances at each noise-free point are calculated using 500 realizations of noisy tTACs. To determine the associated cluster of the projected tTACs of A, the Mahalanobis distance between the point and each noise-free point is calculated, and then, the nearest point is selected. In our example, this is C_1. Finally, the

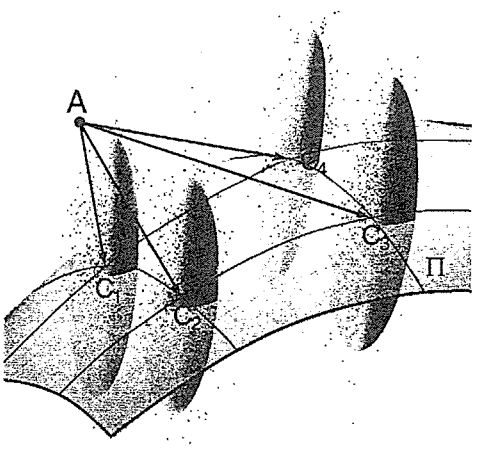

Fig. 1. A semantic diagram for parameter estimation using the proposed MAP-based algorithm. Π is a feature surface, and C_1–C_4 are the projected noise-free tTACs. Noisy projections are denoted by the smaller plots, and the estimated Gaussian is denoted by the superimposed ellipsoid. If a voxel-based tTAC is projected on A, then the Mahalanobis distance to each noise-free point can be calculated ($\overline{AC_1}$–$\overline{AC_4}$). Then, A can be classified as belonging to the nearest point of C_1.

corresponding values of k_2 and k_3 to the point are taken to be the estimates of the voxel-based tTAC. The ratio of the integral of the voxel-based tTAC to that of the corresponding noise-free tTAC determines the value of k_1.

Simulation

A simulation study was designed to determine the appropriate dimensionality of a feature space based on an estimation performance, and to validate the estimates using the proposed method. A clinically measured pTAC was applied to Eq. (1) with a set of k_1, k_2, and k_3 values varying from 0.01 to 0.19 with a step size of 0.02, from 0.01 to 0.28 with a step size of 0.03, and from 0.01 to 0.1 with a step size of 0.01, respectively. For each set of the parameters, 27 realizations of noise-free tTACs were generated, and Gaussian noise was added to simulate a real measurement situation. The proposed approach was applied, and the performance was evaluated to compare the data with the real values. Also, Patlak plot was employed to derive the estimates of k_1/k_2 (=DV) and the cerebral metabolic rate of glucose (CMRGlc) computed as:

$$\mathrm{CMRGlc} = \left(\frac{\mathrm{Gl}}{\mathrm{Lc}}\right) K_i \text{ where } K_i = \frac{k_1 k_3}{k_2 + k_3} \tag{6}$$

Gl is glucose content in blood, and Lc is a lamped constant of 0.42. In Patlak plot, the linear relation is established some minutes later after the administration:

$$\frac{C(t)}{C_\mathrm{p}(t)} = K_i \frac{\int_0^t C_\mathrm{p}(u)du}{C_\mathrm{p}(t)} + (\mathrm{DV} + \mathrm{Bv}) \tag{7}$$

where Bv denotes a blood volume. Therefore, the gradient and y-intercept gives us the estimates of CMRGlc and DV (Patlak et al., 1983).

Dimensionality

A dimensionality of feature space was decided using two ways: a performance-based approach as described in Simulation and a theoretical approach. Morgera (1985) proposed a covariance complexity based on an information theory, and it was calculated using the eigenvalues of an inputted data as defined in (Watanabe et al., 2003):

$$\sigma_j = \frac{\lambda_j^2}{\sum_{k=1}^{M} \lambda_k^2}, \tag{8}$$

$$\Gamma_M = -\frac{\sum_{j=1}^{M} \sigma_j \log \sigma_j}{\log M}, \tag{9}$$

where Γ_M denotes the complexity at the dimension of M, and λ_j is the jth eigenvalue of the covariance matrix of C_A sorted in descending order. Γ_M ranges on [0 1], and it represents a uniformity of information derived if M-dimensional feature space is employed. If all axes defining a feature space have almost the same amount of information, $\sigma_j \simeq 1 / M$, and Γ_M approaches to 1. Conversely, if only the first few axes have most information, the corresponding σ_js become almost 1, and $\Gamma_M \simeq 0$.

To investigate the dimensionality, voxel-based tTACs were generated the same as that described in Simulation with 500 realizations. k_1 was fixed at the typical value, and k_2 or k_3 varied in the range of their typical values ±50%. The values were 0.102, 0.130, and 0.062, respectively (Huang et al., 1980). Also, K_i varied in the range of 0.0334 ± 50% with the fixed k_1.

Clinical image

The proposed method was applied to clinical PET scans: five normal volunteers (four males and one female, average age = 22 ± 1.9), and two patients with congenital glucose transporter-1 deficiency (Pascual et al., 2002) (an 11- and a 7-year-old boy) to validate the algorithm in normal and higher than normal cases. The FDG doses injected were 233 ± 19 MBq for the normal subjects, and 155 or 121 MBq for the deficiency patients. The Ethics Committee of the Tokyo Metropolitan Institute of Gerontology approved the study protocol, and informed consent was given by all subjects. The scans were performed using a HEADTOME V apparatus (Shimadzu Corporation, Kyoto, Japan) with arterial blood sampling. The PET images were reconstructed at a resolution of 7.5 mm FWHM, with 128 × 128 voxels and 30 slices with 2 × 2 × 6.25 mm in a voxel size, using a standard convolution back-projection algorithm. Corrections were applied for dead time, detector nonuniformity, and for photon attenuation. The frame-time sequence was 10 s × 6, 30 s × 3, 60 s × 5, and 150 s × 5, and 300 s × 8. Besides, the images obtained from a 57-years-old female Alzheimer patient were formed using a HEADTOME-IV apparatus (Shimadzu Corporation, Kyoto, Japan) with 128 × 128 and 7 slices with 2 × 2 × 13 mm in a voxel size. The frame arrangements were 30 s × 2, 60 s × 4, 120 s × 4, 240 s × 8. The dose was 210 MBq. Parametric images of DV, CMRGlc were then computed. The delay between the tTAC and pTAC data was estimated using the tTAC averaged over all the regions of interest (ROIs) in a round-robin fashion (Kimura et al., 2004), and it was removed from voxel-based tTACs before applying the proposed method. Eq. (1) was fitted to the tTAC using the interior-reflective Newton method (Coleman and Branch,

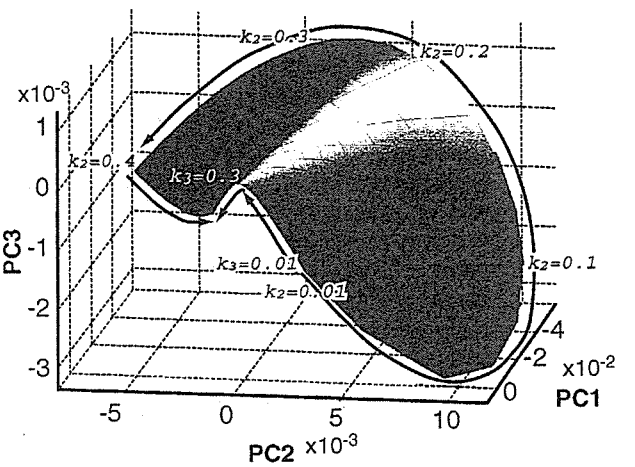

Fig. 2. Example of a feature surface generated in a three-dimensional space. Each axis denotes the first three principal components calculated from a given set of noise-free tTACs. Noise-free tTACs are projected onto this space and form a surface, as shown in the figure. The increase in the values of k_2 and k_3 is denoted by the black and gray arrows, respectively.

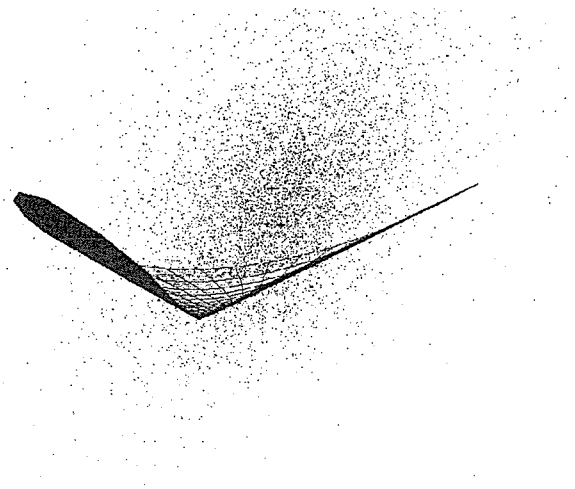

Fig. 3. An actual example of a feature surface and a projected tTACs. The projections are denoted by the small points. The surface is viewed from a low angle to emphasize its curled shape.

1999) with a nonnegative constraint. The initial estimates of all the parameters were selected to be 0.10. The blood volume was fixed at 0.03 (Martine et al., 1987). Before applying the proposed method to clinical data, blood volume component was also subtracted from voxel-based tTACs assuming the fixed blood volume. Additionally, extracranial voxels were manually excluded before the image formation.

To evaluate the consistency between the ordinary ROI-based model estimation and the estimates derived from the proposed algorithm, seven ROIs were selected: the frontal, occipital, parietal, temporal, cerebral, striatum, and the thalamus, and then the nonlinear estimation algorithm was applied to derive the estimates for the ordinary ROI-based kinetic analysis as described above.

Results

Feature surface

A typical feature surface is shown in Fig. 2, in which the generated tTACs are projected into three-dimensional space. It can be seen that the surface is highly curved as denoted by the black and gray arrows. The noise-free tTAC is represented by the lattice points on this surface, and the (k_2, k_3) parameter pair corresponds to one of these points.

Fig. 3 shows a real situation of feature points formed using measured PET data. The measured voxel-based tTACs are projected onto the feature surface denoted by the dots. The noise of the voxel-based tTAC fluctuated widely around the projected points. However, most of the points were located away from the surface because of the noise-induced fluctuation.

Simulation-based validation

Simulation-based validations are summarized in Fig. 4. For k_1, the estimated median values were almost identical to the true values. Moreover, there was an underestimation in this case, because the lower bars of the boxplots are longer than the upper bars. For k_3, the median value was almost the same as the true values, but the distribution of the estimates of k_3 was more complicated than that of k_1. In the case of smaller values of k_3, i.e., $k_3 < 0.03$, the estimate tends to be high. For values of k_3 larger than 0.08, the estimate was lower than the true value. For k_2, a linear

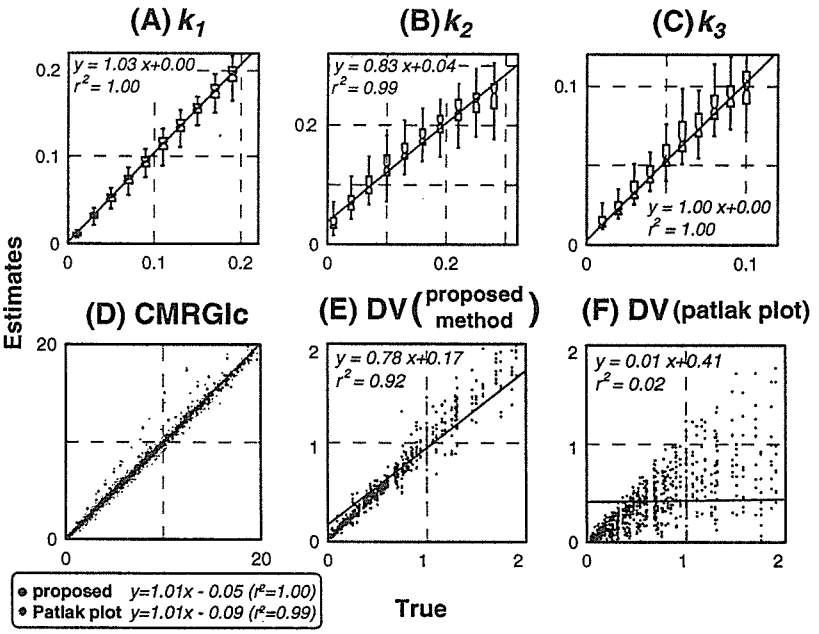

Fig. 4. Performance of the proposed algorithm in a simulation study. The estimates of k_1, k_2, and k_3 are plotted in panels A, B, and C, respectively. The estimates are plotted with respect to the true values as a boxplot. The lower, middle, and upper edges denote the 25th, 50th, and 75th percentiles, and the range shown between the lower and upper ticks is 1.5 times the quartile range, where most data exist. Regression lines between the true and the median are superimposed. CMRGlc estimated by the proposed algorithm and Patlak plot is plotted in panel D with black and gray points, respectively. And estimated DV using the proposed algorithm and Patlak plot is presented in panels E and F. For CMRGlc and DV, the estimates are plotted versus the true values. The regression lines are also shown.

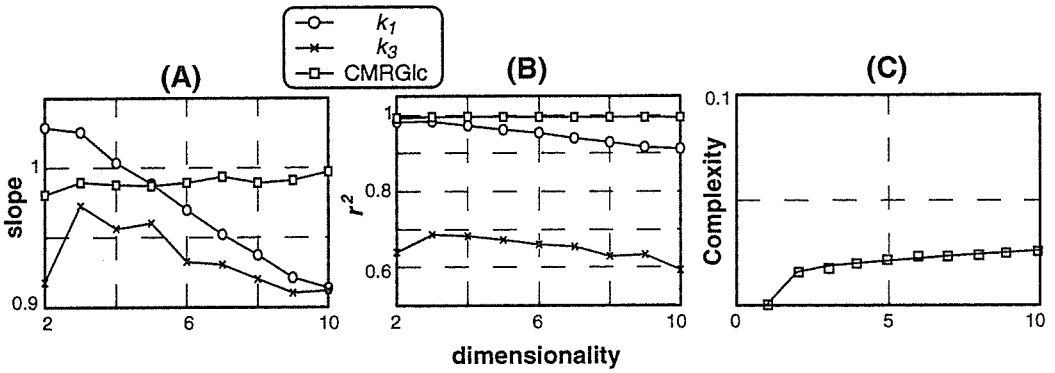

Fig. 5. Courses of a performance and complexity according to dimensionality. The performance comparisons according to the dimensionality of the feature space are shown in Frame (A), the change in consistency between the estimates and their true values, and in Frame (B), the change in linearity. For both quantities, the ideal values are 1. The typical change of covariance complexity is displayed in Frame (C).

relation was maintained, but it was 20% underestimated especially in large k_2 region. For CMRGlc shown in Fig. 4D, both estimates by Patlak plot and the proposed approach were almost identical with the true values, and the estimates from the proposed algorithm presented slightly better estimates. DV estimates showed different states between the proposed algorithm and Patlak plot in Figs. 4E and F. The proposed algorithm gave lineally correlated estimates, on the other hand in Patlak plot, no linear relation with the true DV could be found. The estimates using the proposed algorithm have 22% underestimation in the range of DV between 0 and 2.

Dimensionality

Performance comparisons against the dimensionality are shown in Figs. 5A and B. Frame (A) shows the change in slope of the regression lines between the estimates from the proposed algorithm derived for various dimensions and true values, where a slope equal to unity is the ideal case. For the CMRGlc data, there was no observed dependency on the dimensionality. For k_1, a higher dimensionality leads to an underestimation, and either two or three dimensions seem to be the optimum choice. For k_3, underestimation occurred with two dimensions or more than six dimensions. Frame (B) shows the calculated regression coefficients. The CMRGlc estimates always correlated well with the true values. The performance of the k_1 and k_3 estimates became gradually worse with increasing dimensionality. Three dimensions was the optimum choice based on the estimation performance.

The typical trend of covariance complexity is available in Frame (C) in cases of $k_1 = 0.102$, $k_2 = 0.13$, and $k_3 = 0.062$. Most information concentrated on the 1st dimension because the complexity was near its minimum of 0, and a large increase was observed only at the dimension of 2. And, further dimension in the feature space has approximately a uniform amount of information because the complexity gradually grew, but no peaks were observed according to the increase of dimensionality. These results implied that the information was not gained if higher dimensional feature space than 4 was utilized. This disposition was common in all k-parameters.

Clinical image

ROI-based validations are shown in Figs. 6 and 7, and typical clinical images are available in Fig. 8. For k_1, if it was smaller than 0.16 (which is normal range), the regression line was $y = 0.97x + 0.04$ ($r^2 = 0.90$); this line is plotted in a solid line in Fig. 6A, and both estimates were almost identical. However, the linear regression derived from all k_1 range was $y = 0.73x + 0.03$ ($r^2 = 0.96$), the dashed line in Fig. 6A, and 27% of underestimation was observed. For k_3 shown in Fig. 6C, if $k_3 < 0.13$ (the normal range of k_3), $y = 0.78x + 0.01$ ($r^2 = 0.92$), the solid line, and 22% of underestimation existed. The linear regression in all k_3 range was $y = 1.00x - 0.01$ ($r^2 = 0.91$); an almost identical relation. k_2 is summarized in Fig. 6B. The relation was $y = 0.57x + 0.12$ ($r^2 = 0.88$). For CMRGlc and DV, the comparisons between an ROI-based nonlinear estimation and the proposed algorithm or Patlak plot are illustrated in Fig. 7. Both CMRGlc estimates had good linear relations with 10% of underestimation as shown in CMRGlc-1 and CMRGlc-2; $y = 0.90x + 0.21$ ($r^2 = 0.98$) for the proposed algorithm and $y = 0.91x - 0.012$

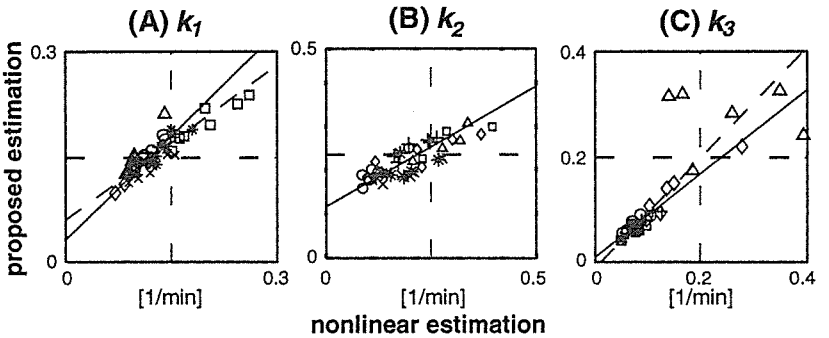

Fig. 6. Comparison between ordinary ROI-based nonlinear estimates and the proposed algorithm. Seven ROIs were placed on seven subjects, and subjects are plotted with different symbols. Regression lines derived from ordinary parameter range and from all estimates are plotted in solid and dashed lines, respectively.

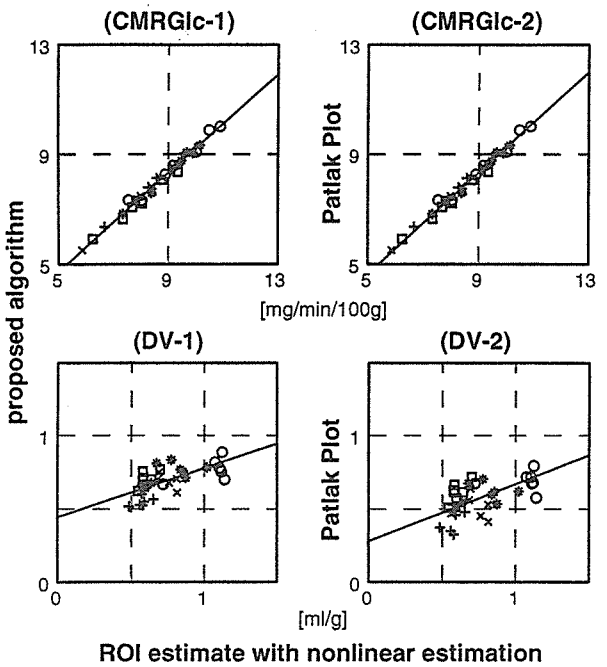

Fig. 7. Comparison between ordinary ROI-based nonlinear estimates and the proposed algorithm or Patlak plot on CMRGlc in (CMRGlc-1) and (CMRGlc-2), and on DV in (DV-1) and (DV-2). (CMRGlc-1) and (DV-1) were derived from the proposed algorithm, and (CMRGlc-2) and (DV-2) represent the estimates using Patlak plot. Seven ROIs were placed on seven subjects, and subjects are plotted with different symbols. Regression lines are superimposed.

($r^2 = 0.97$) for Patlak plot. The deviation of CMRGlc estimates with the proposed algorithm was 8% smaller than that with Patlak plot in the ROI-based validation. The relation of DV is not good; $y = 0.33x + 0.44$ ($r^2 = 0.96$) for the proposed algorithm and $y = 0.39x + 0.28$ ($r^2 = 0.97$) for Patlak plot in DV-1 and DV-2. The simulation showed that k_2 and DV had relatively poor linear relation and 20% of underestimation in Fig. 4, and the same results can be seen in the clinical results (Figs. 6B and 7DV-1). Also, the bias in DV estimates was not ignorable. Patlak plot can estimate DV, but it was poor as the proposed algorithm. The deviation of DV estimates by the proposed algorithm was around 35% smaller than those by Patlak plot in the ROI-based validation. However, in Fig. 8, the gray and white matter can be distinguished in the Alzheimer case, and also in the normal case because there was a monotonous relation between the DV estimates by the proposed algorithm and the ROI-based estimates. The performance of the proposed algorithm was rather sufficient for DV imaging. For CMRGlc, both estimates coincided well with each other. Generally, there is a good linear relation between both estimates in all parameters, and the CMRGlc and k_1 in its normal range were almost identical with the true values.

In the normal case in Fig. 8, the slices shown include the cerebellum and the thalamus. The brain structure is clearly visualized in the CMRGlc image, and in the k_1, k_3, and DV images. Some regional differences in glucose metabolism are observable: the cerebellum has a higher k_1 value than the cerebral cortex, and the k_3 value of the cerebellum is smaller than that in the cerebral cortex. In Alzheimer case, CMRGlc is clearly defected on the right temporal lobe. k_1, k_3, and DV are also lower than those in the left side. For CMRGlc, both methods give us a good brain structure, and the images with the proposed algorithm are less noisy than those with Patlak plot. For DV, the brain structure is unclear in the image with Patlak plot; however, the gray and white matter can be recognized in the proposed method.

It took about 10 min to generate a parametric image composed of 128 × 128 voxels and 30 slices using an Ultra-80 Workstation equipped with a 450 MHz Ultra SPARC-II processor and 4 gigabytes of memory (Sun Microsystems, Santa Clara, CA, USA), in which around 5 min was taken to generate the feature space and to calculate the covariances.

Discussion

We have discussed a novel scheme for voxel-based compartment model analysis methodology. Four points are covered in the discussion: the specificity of the algorithm to form a parametric image, a comparison with other methods for parametric imaging, the development of a MAP-based algorithm, and the performance and usability of the proposed approach.

We now discuss the difficulties encountered in parametric image formation using PET. PET can measure various functionalities in living tissues using a compartment model analysis. If the analysis is applied in a voxel-by-voxel fashion, then a functional image can be derived. Unfortunately, there are two serious drawbacks in voxel-based kinetic analysis. One is a high noise factor in voxel-based tTACs, and the other is the large calculation time required. The small volumes in voxels cause the high noise seen in voxel-based tTACs, and this leads to statistical uncertainties in the estimated kinetic parameters. If a nonlinear estimation algorithm is applied, then voxel-based parameter estimations tend to include large estimation variances and/or erroneous results because of this nonconvergence. Furthermore, a nonlinear estimation algorithm involves a considerable calculation time. The algorithm is usually implemented using an iterative approach, and typically, a compartment model analysis requires several dozen iterations. Additionally, a convolution operation is necessary to calculate a predicted output using a measured pTAC and interim parameters in these iterations, which is time-consuming. To make matters worse, the number of voxels can reach up to half a million. A PET camera has 128 × 128 voxels per slice, and can capture over 30 slices, giving a total of 5×10^5 voxels. For parametric image formation, the model estimation algorithm should be invoked at each voxel, so a huge calculation time is required. If it requires 10 s to obtain one voxel-based parameter estimation, then a couple of months will be required to form a parametric image. The above considerations make functional imaging in PET impractical.

The proposed approach is designed to overcome these problems using MAP algorithm. The model parameters are determined based on their proximity in the shape of a tTAC between a measured voxel-based tTAC and tTACs located in the bank of noise-free tTACs. The proposed approach tries to find most matched noise-free tTAC for a given feature space. Accordingly, the proposed approach does not invoke any parameter estimation algorithm, and the problems regarding parameter estimation and calculation time are therefore resolved.

The dimensionality of a feature space must be given a priori, because it defines the experimental space. In this study, an optimal

dimensionality was decided by using the simulation for validation method and a covariance complexity based on an information theory, as shown in Fig. 5. In the result, three dimensions were chosen as the optimum choice. The number of estimated parameters used was two: k_2 and k_3, because k_1 was ignored as shown in Eq. (3). This implies that a dimensionality higher than two is desirable to consider the noise in a tTAC. Moreover, the dimensionality must also be decided to take into account the signal-to-noise ratio. In Fig. 3, the projections were not located around the feature surface, but were widely scattered. This situation means that considerable noise was present. If the dimensionality used were too high, then a defined feature space would be composed of noise rather than the tTAC.

A covariance complexity denotes a uniformity of information in a given dimensionality and each axis defining a feature space. If the complexity is near 0, most information concentrates on first some axes. The result conveyed that the feature space was governed by the first some principal axes because the complexity was low; its maximum was 1.0 because of the definition, and it was smaller than 0.1 in all range of dimensionality. And, the complexity was increased at the dimension of two as shown in Fig. 5C, which represents that a new information can be expected if the 2nd axis is incorporated. In our performance-based simulation, at higher dimensions, the estimates were too low, and the linearity diminished. On balancing the number of parameters and quality of the input signal, three dimension remains the optimum choice. In the proposed algorithm, projected feature points are classified to multiple categories corresponding to pairs of k_2 and k_3 laid in a physiologically possible range. It is a complicated situation, and both information theory and performance-based indices are reasonable choices to decide the dimensionality for feature space definition.

We also compared the proposed method with other algorithms for voxel-based estimation. Some approaches linearize the compartment model to simplify the estimation process. Logan plot (Logan et al., 1996) and Patlak plot (Patlak et al., 1983) are popular algorithm choices for this operation, which uses a line estimation algorithm. RPM (Gunn et al., 1997) is another widely used algorithm used to visualize the binding potential using a spectrum approach. These algorithms are computationally simple and are therefore fast, because they are implemented with a linear estimation algorithm or a search for a minimal residual point from a table, and an iteration and convolution are not required. However, these algorithms can estimate only limited parameters: a distribution volume, an influx parameter, or a binding potential. Furthermore, the applicability of these algorithms depends on the

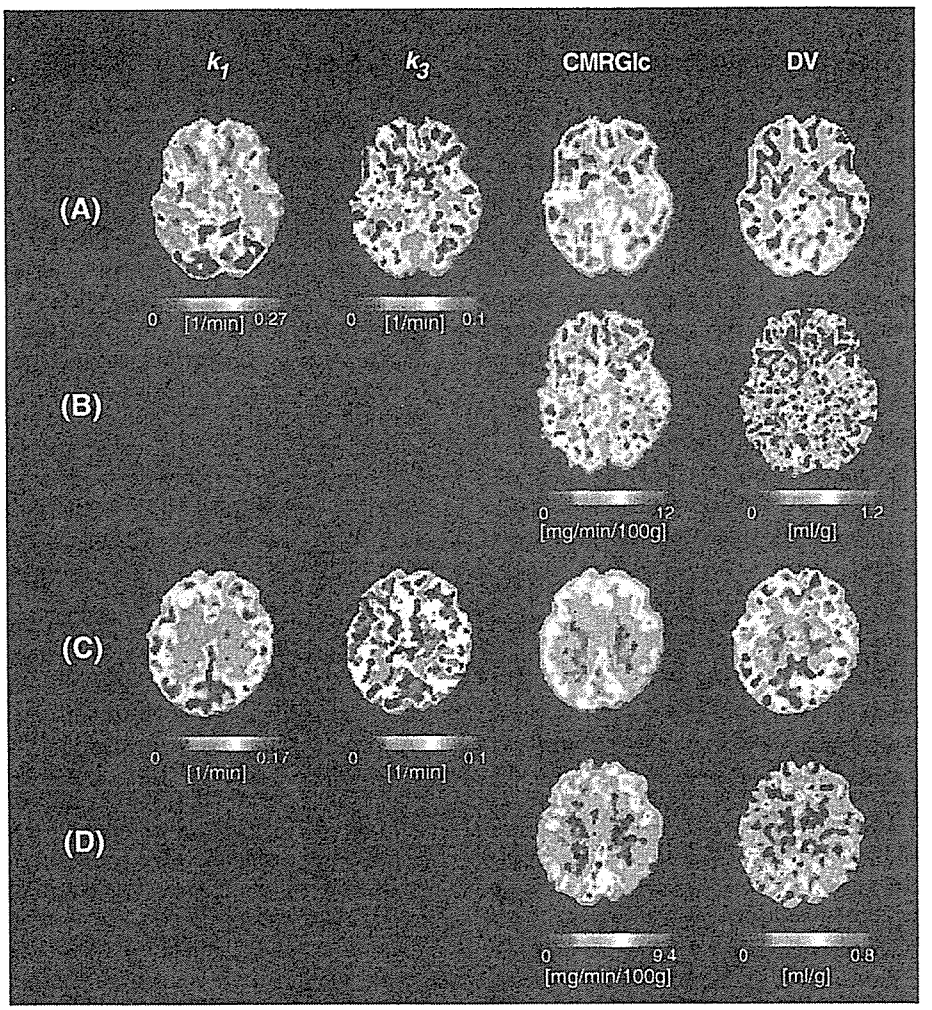

Fig. 8. Clinical images of glucose metabolism in a normal young female in panels A and B, and Alzheimer patient in panels C and D. Panels A and C were derived from the proposed algorithm, and panels B and D were formed by Patlak plot. All images were processed with a median filter.

kinetics of an administered radiopharmaceutical. Because FDG is trapped in a cell, then Logan plot and RPM are not applicable, but using Patlak plot is feasible. In contrast, the proposed algorithm can estimate all kinetic parameters, and is applicable to any compartment model, because the proposed approach is based on a general compartment model, and there is no assumption involved in the model kinetics. Likewise, for determination of optimal estimates, the method searches the nearest feature point instead of invoking nonlinear optimization algorithm which is usually utilized for a compartment model estimation. Accordingly, the proposed algorithm is computationally simple and fast.

We now consider the method based on statistical approach for medical image processing. An interesting study is the mixture analysis approach (O'Sullivan, 1993). O'Sullivan assumed tTACs as a weighted sum of sub-tTACs extracted from a dynamic data using a clustering algorithm. Clustering for PET data analysis was summarized in O'Sullivan (1994). Averaging dynamic data in voxels that belong to the same cluster improves the signal-to-noise ratio in voxel-based dynamic data, and it is helpful for parametric image formation (Kimura et al., 1999; Kimura et al., 2002; Kimura, 2004; Bentourkia, 2001; Wong et al., 2002; Bal et al., 2004; Guo et al., 2003). Additionally, it can reduce the number of data to be analyzed, and makes parametric image formation practical (Kimura et al., 1999; Kimura et al., 2002).

In Kimura (2004), an unsupervised clustering approach was implemented using a Gaussian mixture model. However, because of the large volume of data, the clustering algorithm used was rather unstable for convergence. In the proposed algorithm, MAP approach was introduced. The concept of MAP is that a priori knowledge is incorporated in order to develop the performance for parameter estimation. In MAP, an object function to be maximized for parameter estimation is composed as a sum of a likelihood and a priori probability (Sparacino et al., 2000). Various ways were proposed to define a priori knowledge: using maximum-likelihood estimates for the analysis of glucose contents in the blood (Sparacino et al., 2000), or using population-based values (Callegari et al., 2002), applying population-based averaged values to estimate FDG PET data (Bertoldo et al., 2004), including physiological constraints as a penalty term in an object function for model estimation (O'Sullivan and Saha, 1999) which can reduce estimation variance significantly for FDG imaging, and the approach was extended to spectral analysis (Trukheimer et al., 2003). In the method, a flat prior was defined in a parameter space which means that all parameters have even possibilities, and the Mahalanobis distance was introduced to realize MAP estimation using measured likelihoods derived from random sampling scheme.

The performance and usability of the proposed approach technique is now discussed. Both simulation and clinical studies showed that the estimates using the proposed algorithm approach were very close to, or had a linear relation to either the true parameters (Fig. 4) or to the ROI-based ordinary kinetic results (Figs. 6 and 7). The estimated CMRGlc data always coincided with both the true values and the ROI-based kinetic data, which are shown in Figs. 4D and Fig. 7 CMRGlc-1. In the CMRGlc image shown in Fig. 8, some cortical structures between the gray and white matter were well visualized, and the thalamus could be identified. For the k_1 data, the performance depended on the value used. In the range $k_1 < 0.16$ (the expected normal range of k_1), the estimate was almost identical, shown by the solid line in Fig. 6A. In addition, there was a 27% underestimation for larger k_1 values, shown by the dashed line in Fig. 6A. However, it can be said that the estimates are linearly correlated with the ROI-based kinetic results for all ranges of k_1. The performance of k_3 was worse than that of k_1. In the expected normal range of k_3, i.e., $k_3 < 0.13$, the estimate was 27% underestimated from the results of the ROI-based kinetic analysis. For higher values of k_3, the estimates had almost identical values with the ROI-kinetics. Moreover, for all ranges of k_3, a linear relation existed.

CMRGlc and DV were compared with Patlak plot in Figs. 4 and 7. Patlak plot is a well-established graphical approach which enables voxel-based calculation of both quantities. For CMRGlc, these two methods can offer good estimates and they were almost identical with an ordinal ROI-based kinetic analysis. While for DV, a situation was worse. The DV by the proposed algorithm was largely underestimated and only weak linear relation could be found. In clinical images of CMRGlc and DV in Fig. 8, the images derived from the proposed algorithm were less noisy than those made by Patlak plot especially in DV images; the estimation deviations derived from the proposed algorithm were 8% and 35% smaller than those of Patlak plot for CMRGlc and DV, respectively. Patlak plot calculates DV as a y-intercept, and it is sensitive for an estimation variance in a gradient of the plot. In the proposed approach, noise propagation in a voxel-based tTAC is considered as a likelihood function on the feature surface, and it might contribute an image quality developed.

Usually in FDG PET study, only CMRGlc is utilized for clinical purposes because a CMRGlc image contains some information for brain pathophysiology and it is easy to measure. Some previous works concluded that glucose transporters (Kalaria and Harik, 1989) and a clearance rate of glucose (Feinendegen et al., 2001) were affected by Alzheimer disease or cerebral infarction. Kalaria (Kalaria and Harik, 1989) reported that the hexose transporter located in the brain capillary was significantly decreased in Alzheimer patients. Also, k_1 images in Alzheimer patients have lower parts in the temporal lobe as shown in Fig. 8. They suggested that there is potential usefulness for the study of cerebral metabolism, and the method for voxel-by-voxel compartment model analysis should be developed. In the images in Fig. 8, the brain structure was well visualized, and a defect part in Alzheimer case is available. Fig. 8 showed that the glucose transportation was not homogeneous, and that it was higher in the cerebellum than in the cerebral images. Moreover, the images on cerebral glucose metabolism have different appearance between normal and Alzheimer case. This supports potential for more clinical application.

The overestimation and underestimation values speculated to originate from the distorted shape of the feature surface are shown in Fig. 2. The surface has a topologically quadrangular shape, but it is mostly curved. In the case of large k_3 values, the surface becomes narrow, and the projections of the measured voxel-based tTACs fluctuate in a wider range of parameter values than those of smaller k_3 values. This local difference in shape probably influences the different performances in the estimates. Furthermore, k_1 was a constant during generating noisy tTACs to calculate covariances on the feature surface, see Fig. 1, and a variance of tTAC was assumed to be proportional to the true tTAC value. The current algorithm ignores the dependency of noise distribution on an amplitude of tTAC. It would be needed to develop the algorithm in which tTAC amplitudes is considered. Using the proposed method, the noise propagation from the measured tTAC to the kinetic parameters was modeled in a statistical fashion, and it was

successful in realizing reliable estimates. More complicated statistical modeling is possible, but the proposed multivariate Gaussian scheme is a reasonable choice.

In summary, the proposed algorithm provides good CMRGlc images, which are identical to those from ordinary ROI-based kinetic analysis. The k_1 images are almost identical for values in the normal range. Images show underestimated k_3 and DV; however, the contrast is well maintained. The proposed scheme is theoretically expandable to the compartment model analysis for receptor kinetics because of no assumption for compartment model estimation. However, it causes an increase of the number of parameters, and the shape of feature surface becomes presumably more complex. More robust algorithm will be required.

Acknowledgment

This work was partially supported by the Japan Society for the Promotion of Science, Grant-in-Aid for Scientific Research (C), No. 16591243, 2004 and 2005.

References

Bal, H., DiBella, E.V.R., Gullberg, G.T., 2004. Parametric image formation using clustering for dynamic cardiac SPECT. IEEE Trans. Neural Netw. 50, 1584–1589.

Bentourkia, M., 2001. A flexible image segmentation prior to parametric estimation. Comput. Med. Imaging Graph. 25, 501–506.

Bertoldo, A., Spracino, G., Cobelli, C., 2004. Population approach improves parameter estimation of kinetic models from dynamic PET data. IEEE Trans. Med. Imag. 23, 297–306.

Callegari, T., Caumo, A., Cobelli, C., 2002. Generalization of map estimation in SAAM II: validation against ADAPT II in a glucose model case study. Ann. Biomed. Eng. 30, 961–968.

Coleman, T., Branch, M.A., 1999. Nonlinear least-squares. Optimization Toolbox User's Guide. MathWorks Inc., pp. 3–11 (Version 2).

Duda, R.O., Hart, P.E., Stork, D.G., 2001. Bayesian decision theory—Continuous features. Pattern Classification, (Second ed.)John Wiley and Sons, Inc., pp. 24–26.

Feinendegen, L.E., Herzog, H., Thompson, K.H., 2001. Cerebral glucose transport implies individualized glial cell function. J. Cereb. Blood Flow Metab. 21, 1160–1170.

Gunn, R.N., Lammertsma, A.A., Hume, S.P., Cunningham, V.J., 1997. Parametric imaging of ligand–receptor binding in PET using a simplified reference region model. NeuroImage 6, 279–287.

Guo, H., Renaut, R., Chen, K., Reiman, E., 2003. Clustering huge data sets for parametric PET imaging. Biosystems 71, 81–92.

Huang, S.C., Phelps, M.E., 1986. Principles of tracer kinetic modeling in positron emission tomography and autoradiography. In: Phelps, M.E., Mazziotta, J.C., Schlbert, H.R. (Eds.), Positron Emission Tomography and Autoradiography—Principles and Applications for the Brain and Heart. Raven Press, New York, USA, pp. 287–346.

Huang, S.C., Phelps, M.E., Hoffman, E.J., Sideris, K., Selin, C.J., Kuhl, D.E., 1980. Noninvasive determination of local cerebral metabolic rate of glucose in man. Am. J. Physiol. 238, E69–E82.

Kalaria, R.N., Harik, S.I., 1989. Reduced glucose transporter at the blood–brain barrier and in cerebral cortex in Alzheimer disease. J. Neurochem. 53, 1083–1088.

Kimura, Y., 2004. Formation of parametric image with statistical clustering. In: Iida, H., Shah, N.J., Hayashi, H., Watabe, H. (Eds.), Quantitation in Biomedical Imaging with PET and MRI, International Congress Series, vol. 1265. Elsevier, pp. 25–30.

Kimura, Y., Hsu, H., Toyama, H., Senda, M., Alpert, N.M., 1999. Improved signal-to-noise ratio in parametric images by cluster analysis. NeuroImage 9, 554–561.

Kimura, Y., Senda, M., Alpert, N.M., 2002. Fast formation of statistically reliable FDG parametric images based on clustering and principal component. Phys. Med. Biol. 47, 455–468.

Kimura, Y., Ishii, K., Fukumitsu, N., Oda, K., Sasaki, T., Kawamura, K., Ishiwata, K., 2004. Quantitative analysis of adenosine A_1 receptors in human brain using positron emission tomography and [1-methyl-^{11}C]8-dicyclopropylmethyl-1-methyl-3-propylxanthine. Nucl. Med. Biol. 31, 975–981.

Logan, J., Fowler, J.S., Volkow, N.D., Wang, G.J., Ding, Y.S., Alexoff, D.L., 1996. Distribution volume ratios without blood sampling from graphical analysis of PET data. J. Cereb. Blood Flow Metab. 16, 834–840.

Lucignani, G., Schmidt, K.C., Moresco, R.M., Striano, G., Colombo, F., Sokoloff, L., Fazio, F., 1993. Measurement of regional cerebral glucose utilization with Fluorine-18-FDG and PET in heterogeneous tissues: theoretical considerations and practical procedure. J. Nucl. Med. 34, 360–369.

Martine, W.R.W., Powers, W.J., Raichle, M.E., 1987. Cerebral blood volume measured with inhaled C^{15}O and positron emission tomography. J. Cereb. Blood Flow Metab. 7, 421–426.

Morgera, S.D., 1985. Information theoretic covariance complexity and its relation to pattern recognition. IEEE Trans. Syst. Man Cybern. SMC-15, 608–619.

O'Sullivan, F., 1993. Imaging radiotracer model parameters in PET: a mixture analysis approach. IEEE Trans. Med. Imag. 12, 399–412.

O'Sullivan, F., 1994. Metabolite images from dynamic positron emission tomography studies. Stat. Methods Med. Res. 3, 87–101.

O'Sullivan, F., Saha, A., 1999. Use of ridge regression for improved estimation of kinetic constants from PET data. IEEE Trans. Med. Imag. 18, 115–125.

Pascual, J.M., van Heerrtum, R.L., Wang, D., Engelstad, K., Vivo, D.C.D., 2002. Imaging the metabolic footprint of Glut1 deficiency on the brain. Ann. Neurol. 52, 458–464.

Patlak, C.S., Blasberg, R.G., Fenstermacher, J.D., 1983. Graphical evaluation of blood-to-brain transfer constants from multiple-time uptake data. J. Cereb. Blood Flow Metab. 3, 1–7.

Sparacino, G., Tombolato, C., Cobelli, C., 2000. Maximum-likelihood versus maximum *a posteriori* parameter estimation of physiological system models: the C-peptide impulse response case study. IEEE Trans. Biomed. Eng. 47, 801–811.

Trukheimer, F.E., Hinz, R., Gunn, R., Aston, J.A.D., Steve, R., Gunn, V.J.C., 2003. Rank-shaping regularization of exponential spectral analysis for application to functional parametric mapping. Phys. Med. Biol. 48, 3819–3841.

Watanabe, T.A.A., Cellucci, C.J., Kohegyi, E., Bashore, T.R., Josiassen, R.C., Greenbaun, N.N., Rapp, P.E., 2003. The algorithmic complexity of muitichannel EEGs is sensitize to change in behavior. Psychophysiology 40, 77–97.

Wong, K.P., Feng, D., Meikle, R., Fulham, M.J., 2002. Segmentation of dynamic PET images using cluster analysis. IEEE Trans. Med. Imag. 49, 200–207.